Characterization of Biomass Materials for Understanding the Processing

by

Zijian Ma

A Thesis

Submitted to the Faculty

of the

WORCESTER POLYTECHNIC INSTITUTE

in partial fulfillment of the requirements for the

Degree of Master of Science

in

Chemical Engineering

April 2017

Table of Contents

Executive Summary

Biomass is the most important source of renewable energy in the industrial sector, and it plays an essential role in providing byproduct energy for the pulp and paper industry.[1] In 2016, 10,146 trillion btu of biomass was produced and 4,754 trillion btu was consumed, the consumption occupies around half of the total renewable energy.[2] Biomass can be obtained from terrestrial and aquatic plants, human and animal solid wastes and etc.[3] Utilization of biomass includes direct combustion, biochemical processing and thermochemical processing. Va´rhegyi et al.[4] studied the pyrolysis and combustion property of macadamia nutshell and eucalyptus wood for process development of charcoal yielding. Yang et al.[5] suggested an optimized condition for maximum production of oil and energy in liquefaction of algae. Kim et al.[6] studied a methane fermentation system to digest food waste at different temperatures and retention time.

Characterization is one of the most important steps to understand the response and reaction of biomass during processing. A variety of techniques are used to characterize the biomass materials and track its changes including scanning electron microscope, mass spectrometry and etc., which is hard to review all here. However, several techniques have attracted the most attention and been used frequently such as vibrational spectroscopy (Infrared spectroscopy and Raman spectroscopy) and thermogravimetric analysis (TGA). Infrared spectroscopy was applied by Watanabe et al.[7] to investigate the water adsorption onto microcrystalline cellulose, the results indicate the inter- and intrachain H-bonds are formed by monomeric water molecule adsorption and 3-7 wt % absorbed water affects the H-bonds network at the interface. Agarwal et al.[8] employed Raman spectroscopy to reveal the structure of wood cell wall cellulose, the native cellulose is turned out to be less than crystalline state and the internal chains of laterally aggregated cellulose are water-accessible. Pyrolysis kinetics of three wood materials were studied by

thermogravimetric analysis, the theoretical kinetic models and apparent activation energy were obtained for the main components, cellulose and hemicellulose. [9]

In this work, vibrational and thermal behavior of several important systems were studied. The first study was a measurement of the infrared vibrational spectra of glucose and two important glucose dimers (cellobiose and maltose) as a function of temperature. The purpose of his study was to measure shifts in vibrational band positions to gain insight into carbohydrate reactivity. The second study was on hydrothermally treated coffee waste biomass. Here, collaborators at University of Campinas (UNICAMP, Brazil) treated coffee waste biomass in a flow-through subcritical water hydrolysis reactor. The purpose of the M.S. study on coffee waste was to understand the chemical changes that occurred to the residual solids during hydrolysis treatment. Vibrational spectroscopy and thermal analysis techniques were used. The third and final study was to understand the chemical composition of the solid product resulting from co-solvent enhanced lignin fractionation (CELF) of several biomass feeds. Collaborators at University of California Riverside (UCR) recently developed the CELF process. The purpose of the M.S. study on the CELF solid product was to understand its composition to help guide the CELF reactor design and determine applications for the CELF solids. Taken together, the 3 studies are integrated into a cohesive whole that demonstrates the use of spectroscopic and thermal techniques for characterizing biomass and understanding its composition at the molecular level.

Glucose is an unit of cellulose, structure of which is linked by β (1–4) bond and the two disaccharides, cellobiose and maltose, are two glucose units linked by β (1–4) and α (1–4) bonds respectively. We employed Infrared spectroscopy to study the temperature dependence of the saccharides, the spectra were peak fitted and the temperature variability of O–H band positions

were recorded. The results indicate three O–H bonds of glucose and two of cellobiose are strong temperature dependent, while maltose showed subtle temperature dependence. Investigation on these simple saccharides provides basis to understand processing of cellulose and suggest to design a catalyst which is able to cut the larger temperature dependent bonds first selectively.

Most industrial processing of biomass is conducted in fed batches due to the simple operation, but an advanced flow batch reactor model starts to attract attention because of the benefit of higher yields of hemicellulose and removal of lignin. [10] Mayanga-Torres et al.[11] subjected coffee wastes to a subcritical water flow through reactor to extract reducing sugar and phenolic compounds at different temperatures and pressures. The hydrolysate were analyzed to obtain the highest yield at the best condition. We studied the raw coffee waste material and treated solid residue with elemental analysis, vibrational spectroscopy (Infrared and Raman spectroscopy) and TGA. The carbohydrates were found largely remain and small amount of biochar formed which suggests a surface char shell structure. It's consistent with the low total reducing sugar yield (highest 9 %) and indicates the low efficiency of flow through reactor.

Recently co-solvent enhanced lignocellulosic fractionation (CELF) has been developed as a pretreatment technology that has the potential to solve this problem.[12] Wyman et al. [12] applied a co-solvent with mixture of tetrahydrofuran and dilute acid to achieve higher ethanol yield with lower enzyme loading. We collaborated with them and characterized three wood materials, bagasse, maple wood and poplar wood and their CELF treated residues with TGA, X-ray Diffraction analysis (XRD) and vibrational spectroscopy. They all reflect removal of carbohydrates but still retain indicated by TGA and vibrational spectroscopy. XRD revealed the crystalline index of the raw materials

which can be a guide for choosing the wood candidate. The integrated combination of XRD, TGA and vibrational spectroscopy is a powerful tool to understand the processing of biomass.

Refenrence

(1) U.S. Energy Information Administration. *International Energy Outlook 2016*; 2016; Vol. 0484(2016).

(2) Administration, U. S. E. I. *Monthly Energy Review March 2017*; 2017.

(3) Demirbaş, A. *Energy Convers. Manag.* **2001**, *42* (11), 1357–1378.

(4) Szabo, P.; Till, F.; Antal, M. J.; Dai, X. *Energy & Fuels* **1998**, *624* (6), 969–974.

(5) Yang, Y. F.; Feng, C. P.; Inamori, Y.; Maekawa, T. *Resour. Conserv. Recycl.* **2004**, *43* (1), 21–33.

(6) Kim, J. K.; Oh, B. R.; Chun, Y. N.; Kim, S. W. *J Biosci Bioeng* **2006**, *102* (4), 328–332.

(7) Watanabe, A.; Morita, S.; Ozaki, Y. *Appl Spectrosc* **2006**, *60* (9), 1054–1061.

(8) Agarwal, U. P.; Ralph, S. A.; Reiner, R. S.; Baez, C. *Cellulose* **2016**, *23* (1), 125–144.

(9) Hu, M.; Chen, Z.; Wang, S.; Guo, D.; Ma, C.; Zhou, Y.; Chen, J.; Laghari, M.; Fazal, S.; Xiao, B.; Zhang, B.; Ma, S. *Energy Convers. Manag.* **2016**, *118*, 1–11.

(10) Yang, B.; Wyman, C. E. *Biotechnol. Bioeng.* **2004**, *86* (1), 88–95.

(11) Mayanga-Torres, P. C.; Lachos-Perez, D.; Rezende, C. A.; Prado, J. M.; Ma, Z.; Tompsett, G. T.; Timko, M. T.; Forster-Carneiro, T. *J. Supercrit. Fluids* **2017**, *120*, 75–85.

(12) Nguyen, T. Y.; Cai, C. M.; Osman, O.; Kumar, R.; Wyman, C. E. *Green Chem.* **2016**, 1581–1589.

Chapter I: Infrared Spectroscopic Study of Oligosaccharides – Glucose, Cellobiose and Maltose

Geoffrey A. Tompsett, Zhenyang Yang, Zijian Ma, Avery Brown and Michael T. Timko

Department of Chemical Engineering, Worcester Polytechnic Institute, 100 Institute Rd, Worcester, MA 01609, USA.

Abstract

Temperature dependence of three carbohydrate materials, glucose, cellobiose and maltose were studied employing Infrared spectroscopy. Infrared spectra were obtained at 5 °C interval up to the highest available temperature below the melting point of the materials. The spectra were then deconvoluted by peak fitting with Gaussian curves. The band positions and shifts with respect to temperature of each band were recorded and the O–H region was focused to reveal the temperature response of the chemical groups. Three O–H groups of glucose and two of cellobiose present clear shifts which indicates change of bond length or angle, while those of maltose shift subtly. Molecular modelling of maltose monohydrate assigned each O–H group to a specific frequency. Starting from relatively simple molecular structure which is a unit of cellulose, the study provides basis for understanding vibrational spectroscopy of cellulose.

1. Introduction

Cellulose is one of the most abundant biopolymers on Earth.[1] It is found in most plants (lignocellulosic material), as well as organisms such as algae, in high concentration together with hemicelluloses and lignin.[1] Cellulose is used extensively in the paper, food, chemical and pharmaceutical industries. Biomass carbohydrates are coming under increasing interest as a renewable feedstocks for the production of biofuels and chemicals. The pretreatment and

hydrolysis is a critical step in the economical processing of biomass to bioethanol and other products.[2] Understanding the mechanism of hydrolysis of the glycosidic linkages in oligosaccharides, such as cellulose is of particular importance for the development of new solid acid catalysts and the optimization of these processes. In addition, the glycosidic linkage is also important for understanding its bio–protection abilities.[3] Thermal properties of carbohydrates provides a basis for understanding the decomposition processes. Table 1 summarizes the thermal properties of several important carbohydrates, providing glass transition temperature (T_g), melting point (T_m), decomposition temperature, heat capacity (C_p) and heat of fusion (**ΔH**). [4,5,6,7,8,9,10,11] Heat capacity is a fundamental parameter to obtain other thermal quantitative information.[12] Significant changes happen to physical and chemical properties of carbohydrates above T_g or T_m. Generally, T_g, T_m and C_p increase with higher molecular weight. Tm of maltose monohydrate is relatively lower due to more water content. [5] Most carbohydrates start to decomposite at temperatures slightly higher than the melting point. The melting point and decomposition temperature provides a guide on how high the carbohydrates can be heated up to.

Table 1. Thermal properties of carbohydrates

Carbohydrate	**Tg** (ºC)	**Tm** (ºC)	**Decomposition temperature** (ºC)	**Cp** (J kg^{-1} K^{-1})	**ΔH** ($kJmol^{-1}$)	**Reference**
α–D–Glucose	34	146	>146	334 (410.15K)	36.57 32.22	Lide et al. (1993)[13] Magon et al. (2011)[4] Roos et al. (1993)[5]

Table 1 continued

Carbohydrate	**Tg** (°C)	**Tm** (°C)	**Decomposition temperature** (°C)	**Cp** (J kg^{-1} K^{-1})	**ΔH** ($kJmol^{-1}$)	**Reference**
D–Cellobiose	99	254 and 313 227 (crystalline) 57 (amorphous) 225 236 (241 peak)	235	436.1 (298K)	31.058	Sharma et al. (2014)[6] Roos 1993[5] Hernández–Segura Pinto et al 2010[8]
Maltose (monohydrate)	91	104 160–165 (anhydrous)		1331	43.13	Roos 1993[5]
β–cyclodextrin	225–250	290	308	2104 (undecahydrate) 1372 (anhydrous)		Shimpi et al 2005[9]
I_β cellulose	184 (microcrystalline cellulose) 220 phase change I_β to HT	443 at interface between cellulose and intermediate of short lifetime liquid species (ILC)	>443	2237 for cellulose 4000 for ILC	40 (cellulose to ILC)	Boutin 2002[10] Watanabe 2006[14]

Properties, such as T_g and T_m, are useful for understanding bulk response to thermal conditions, however, they provide no molecular insights. Vibrational spectroscopy has the potential to provide complimentary molecular level information. Stefan et al.[15] employed Raman spectroscopy to study amorphous glucose in the glassy and liquid states over 15 – 55 °C. The spectra and bands were recorded to study how specific chemical group change at different temperatures. Perturbation–correlation moving–window two–dimensional correlation analysis

was applied to understand the overlapping OH bands in the infrared spectroscopy of microcrystalline cellulose[16] Drastic structural changes were found at the glass transition temperature at molecular level. Seo et al.[17] reports temperature dependent Raman spectra of carbohydrates between 50 and 200°C. Seo et al. fit 4–7 bands in the Raman spectral region 1000–1200 cm^{-1} to the spectra at elevated temperatures of trehalose, sucrose and maltose. The origins of the seven peaks fitted to the spectrum of maltose are the (1) C–O stretching, (2) C–O stretching + C–C stretching, (3) C–O stretching + C–C stretching + COH bending, (4) C–O stretching + COH bending + Ring, (5) C–O stretching + CCH bending + Ring, (6) C–O stretching, and (7) C–O stretching + C–C stretching + CCH bending + Ring vibrational modes. Seo et al.[17] found that the location of the glycosidic bond vibration in both trehalose and sucrose changed at temperatures around 120°C, indicating a significant change in the bond length or bond angle (dihedral and torsional angles). In comparison, the band position and hence bond lengths for the glycosidic bond of maltose did not shift significantly.

Although the work above obtained reasonable results and improved understanding of carbohydrates with use of vibrational spectroscopy, Stefan and coworkers[15] only studied at a small range of temperature and Watanabe[16] and Seo et al.[17] only study certain range of the spectra. Our work starts from the whole mid–infrared area, i.e., 4000–400 cm^{-1} over the range from room temperature to the highest available temperature below the melting point of each material.

The molecular information provided by vibrational spectroscopy is dependent on the accuracy of the band assignments. Vibrational bands can sometimes be inferred comparison with known spectra.[18] For complex molecules like saccharides which contain many atoms and functional groups, assignment by comparison with known molecules is often ambiguous.

Computational chemistry has proven to be a useful tool for visualizing vibrational or NMR spectra. [19] Density Functional Theory (DFT) in particular is efficient and accurate to model carbohydrates. [20] Among the methods, B3LYP is a common one with proven accuracy for hydrogen bond interactions.[21] For example, Strati et al. [22] reported that the 6–311++G** basis set was nearly in excellent agreement with experimental geometric structures for several oligosaccharides.

In this paper, we studied the effect of temperature on the vibrational modes of carbohydrates, namely α–D–glucose, cellobiose and maltose (monohydrate) using in situ diffuse reflectance infrared Fourier transform (DRIFTS) spectroscopy. We focused on two main spectral ranges: 3100–3600 cm^{-1} (OH stretching region for hydrogen bonding and 900–1800 cm^{-1} (fingerprint region). The monosaccharide glucose and disaccharide cellobiose and matlose were studied because they are the monosaccharide and disaccharides with the units of cellulose with the same β(1–6) glycosidic bonding. Maltose was also investigated as the disaccharide (one C–O–C bond). 1 unit molecule of a–maltose monohydrate is modelled in vacuum using DFT. The geometry was optimized and the vibrational frequency was calculated to obtain the simulated IR spectrum which facilitates the peak fitting of the experimental spectrum. The assignments for the bands in the O–H region were successfully obtained.

2. Experiments

2.1 Materials

Three carbohydrates, glucose, maltose monohydrate and cellobiose (Sigma–Aldrich), were used without further processing. Thermal properties of them are summarized in Table 1.

2.2 Infrared Spectroscopy

A Nicolet Magna IR–560 FTIR spectrometer was used to obtain infrared spectra and Specac DRIFTS cell was used for in situ measurement. For every spectrum, 512 scans were averaged over 600 – 4000 cm^{-1} range with 4 cm^{-1} resolution. The temperature was controlled from room temperature to the melting point of each material in Table 1. Spectra were obtained at 5 °C intervals. A recirculating chiller (Fisher Scientific) helped cool down the system. The peak fitting is completed by a software Magic Plot which is able to load spectra obtained from the instrument and enable authors to employ Gaussian and Lorentzian curves to fit the spectra underneath it. The resulting fitted spectra shown as dotted line in Figures 5 – 7 are formed by summing up the Gaussian and Lorentzian curves automatically.

2.3 Simulation

2.3.1 Computational methods

Webmo was used for computational modeling of maltose structure and calculating the vibrational spectra. The modelling starts from a small basis set to larger basis sets, which decreases the calculation time efficiently. The method B3LYP is used through all the simulations. The starting molecular structure of maltose was optimized using B3LYP/6–31G(d) based on the Cartesian coordinates reported by Momany et al[23]. The structure was then adjusted with the addition of a water molecule based on the crystal structure of maltose monohydrate provided by Quigley et al.[24] and optimized the structure of maltose monohydrate using the same method and basis set. Two larger basis sets, 6–311+G (2d, p) and 6–311++G**, were then used to optimize and calculate the structure and vibrational frequencies.

2.3.2 Nomenclature

The software Webmo numbers the atoms anti–clockwise presented in Figure 1. The numbering of oxygen atoms are next to that of carbons, so do the hydrogen atoms in the hydroxyl bond next to oxygen atoms. The hydrogen atoms connecting the carbon atoms are numbered afterwards. The carbon in the hydroxymethyl group in the non–reducing glucose unit is numbered (1), and the water is numbered last.

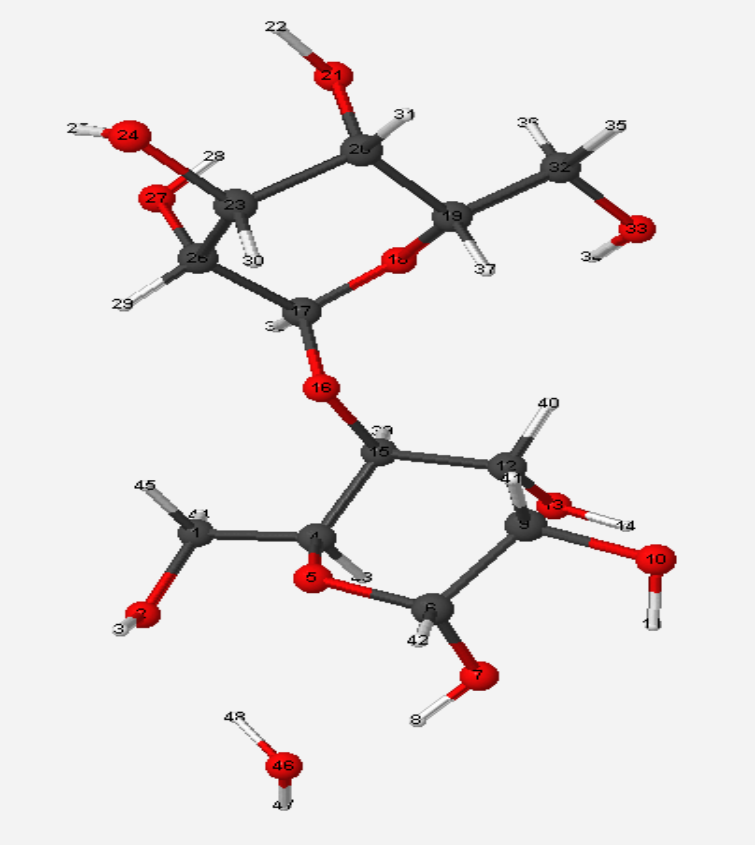

Figure 1. Maltose Monohydrate simulated ending structure with numbering indicated

2.3.3 Spectral Treatment

The peak width is set to 10 cm^{-1}. The intensity and frequency of the simulated spectrum is scaled by 0.9393 to better line up with the experimental one, the intensity of which is also scaled by 0.87.

3. Results and Discussion

3.1 Spectroscopy

We obtained spectra of the carbohydrates at 5 °C intervals over the range 800–2400 cm^{-1} and 2800–3600 cm^{-1}. Figure 2–4 display representative spectra of glucose (Figure 2), cellobiose (Figure 3) and maltose (Figure 4), each at 5 different temperatures. The spectra of each material at room temperature are in a broad agreement with those in the literature on the shape, bands intensity and position with our spectra present a better resolution.[25,26,27] When the cell temperature approaches the melting points, the spectral quality decreases (i.e. , the ratio of signal to noise of the spectra decreases) as the carbohydrates transition into an amorphous state. The molecular structures such as bond length, bond angle and etc. change substantially when carbohydrates transfer to amorphous state, and the bulk materials are transforming to a liquid–like "rubbers" status. Spectra of glucose present fewer bands than that of cellobiose and maltose due to the less complex molecular structure, single ring pyranose compared to the disaccharides in which two glucose units connected by a glycosidic bond. The changes among spectra at different temperatures are more subtle band shifts than intensity change. For instance, the O–H band at around 3450 cm^{-1} blue shifts with temperature increase. The change of spectra of cellobiose is much more complicated than that of glucose. It not only shifts on band positions but also changes on intensity. The spectrum at the highest temperature below melting point is much smoother than spectra at lower temperatures, where many bands disappear. The spectra of maltose change both intensity and band positions slightly. The visual change provides a hint to study them in detail on specific

bands quantitatively in the spectra. Peak fitting method was employed to separate and display the individual sub–bands which contributes to the whole spectrum.

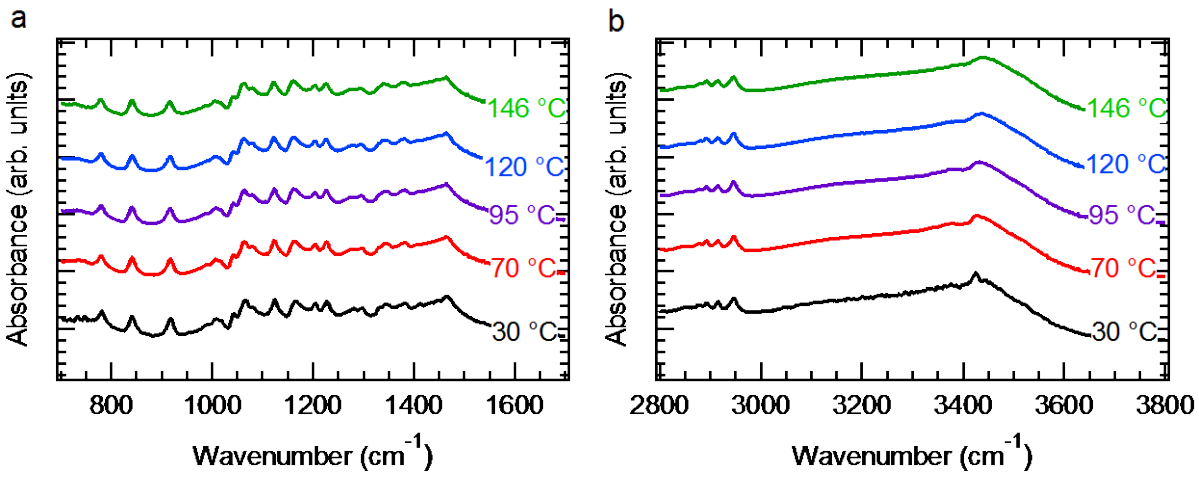

Figure 2. Representative, temperature resolved IR spectra of glucose in dry N_2 over the range (a) 700 cm^{-1} –1700 cm^{-1} and (b) 2800 cm^{-1} –3800 cm^{-1}

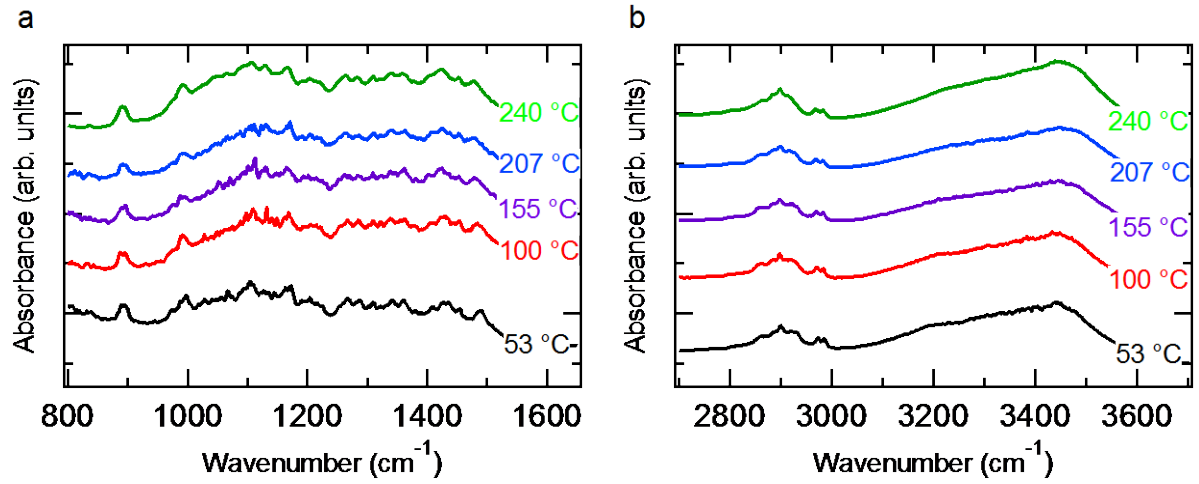

Figure 3. Representative, temperature resolved IR spectra of cellobiose in dry N_2 over the range (a) 800 cm^{-1} –1700 cm^{-1} and (b) 2700 cm^{-1} – 3700 cm^{-1}

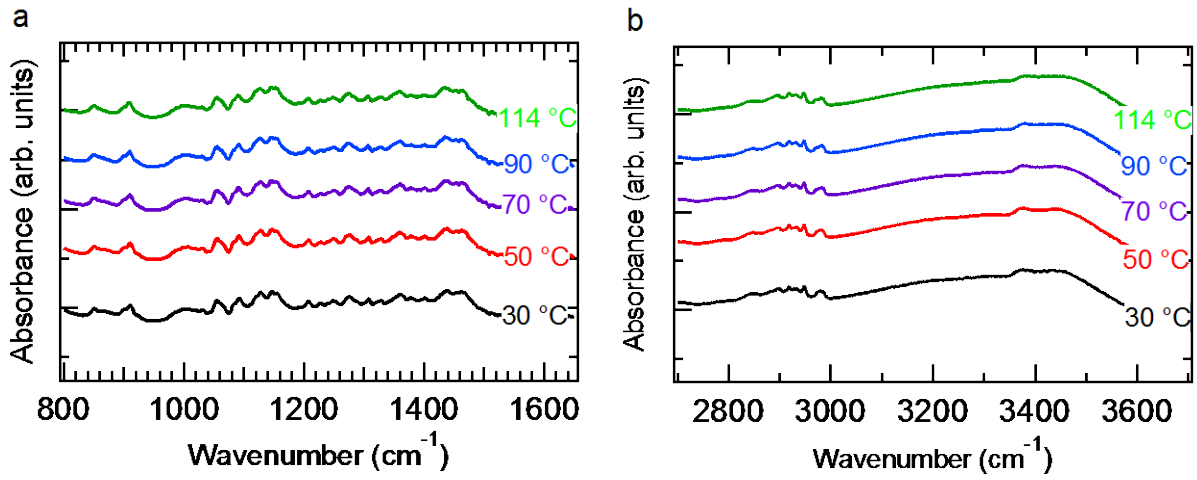

Figure 4. Representative, temperature resolved IR spectra of maltose monohydrate in dry N_2 over the range (a) 800 cm^{-1} –1700 cm^{-1} and (b) 2700 cm^{-1} – 3700 cm^{-1}

3.2 Peak Fitting

To record the temperature variability of specific band positions, the spectra were peak fitted based on previous studies which provided reference band positions in Table 2–4. [28,29,30,31,32] Gaussian curves are used for deconvolution of the spectra and band positions are slightly adjusted from the reference ones to make the resulting fitted spectra consistent with the observed spectra as close as possible. Small adjustment of fitting of spectra at higher temperatures start from the same band position, half–width and area of each Gaussian curve, which are three important parameters assuring the reliability of deconvolution of infrared spectra.[33] The fitting results are shown in Figures 5–7. 20 and 10 peaks were fitted for glucose over the 840 cm^{-1} – 1500 cm^{-1} and 2870 – 3510 cm^{-1} range with 27 at most because of several close peaks and 6 peaks in the literature.[2532] 51 and 6 peaks for cellobiose in the region 890 –1540 cm^{-1} and 3060 –3560 cm^{-1} and 43 and 4 peaks in the literature. [26,34] 33 and 14 peaks for maltose in the region 840 –1460 cm^{-1} and 2700 – 3570 cm^{-1} and 28 and 16 peaks in the literature. [3135] The difference of the amount of peaks in our

peak fitting from that in the literature can be due to instrument and running conditions variance or overlap of fitting bands.[36] However, this won't affect the reliability since the amount of fitting peaks are the same between spectra of the same material and we primarily study the band position shifts among the spectra. The peaks are much more densely spaced over the range from 800 cm^{-1} to 2400 cm^{-1} and have higher resolution than those from 2800 cm^{-1} to 3600 cm^{-1}. Among all the bonds, we are mainly interested in the change of glycosidic bonds (997, 1018, 1070, 1082, 1144, 1154, 1191, 1398, 1407, 1417 and 1456 cm^{-1} for cellobiose and 944, 1056, 1085, 1119, 1179, 1376, 1460 cm^{-1} for maltose) and hydrogen bonds.

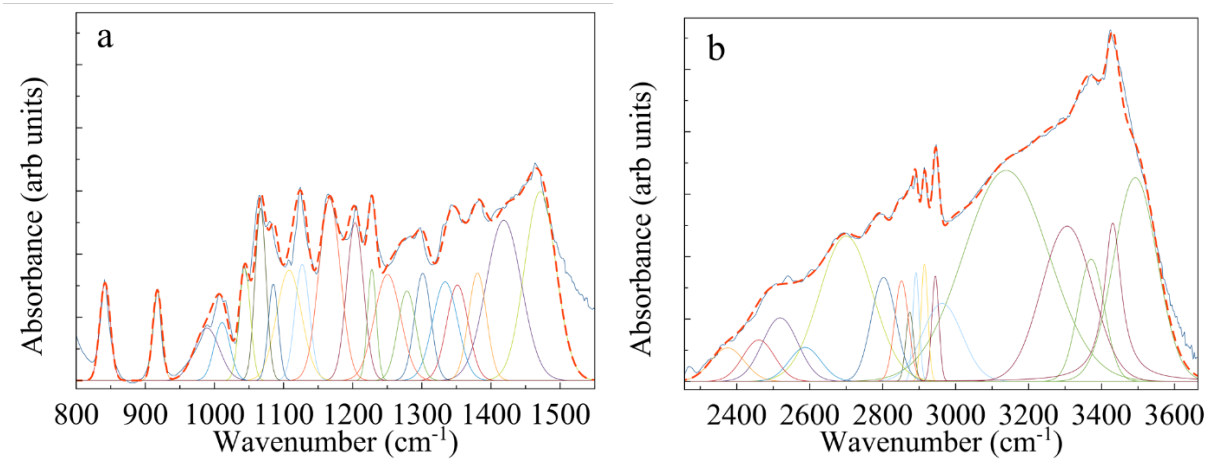

Figure 5. Peak fitting of glucose spectrum at 37°C (a) 800 cm^{-1} –1500 cm^{-1} (b) 2300 cm^{-1} – 3600 cm^{-1}

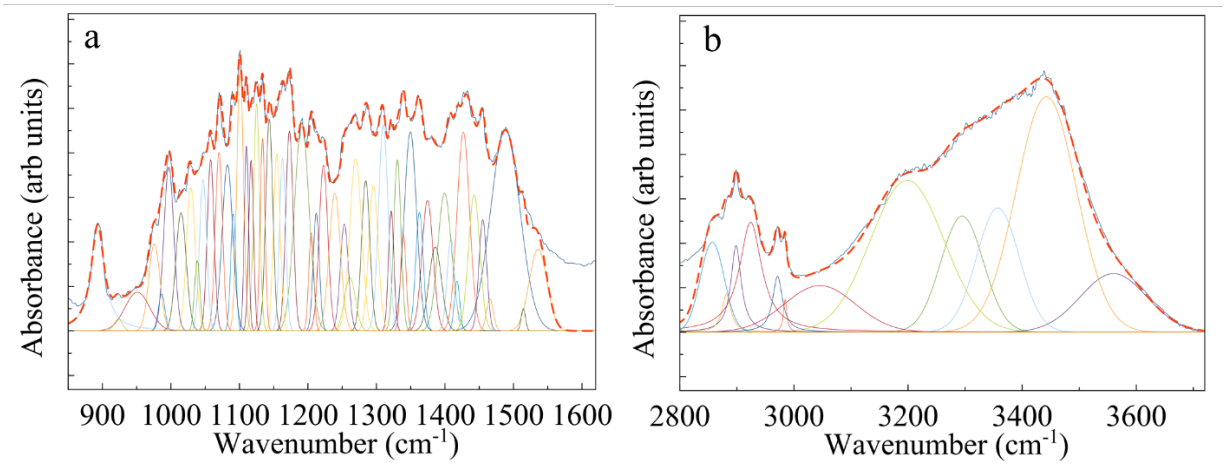

Figure 6. Peak fitting of cellobiose spectrum at 30 °C (a) 800 cm^{-1} –1500 cm^{-1} (b) 2800 cm^{-1} – 3700 cm^{-1}

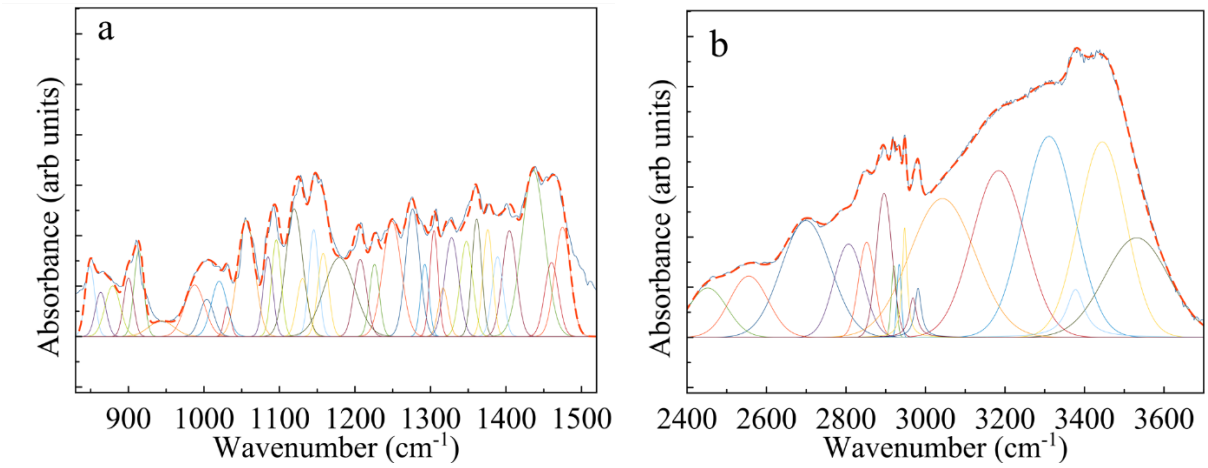

Figure 7. Peak fitting of maltose spectrum at 30 °C (a) 800 cm^{-1} –1500 cm^{-1} (b) 2400 cm^{-1} – 3700 cm^{-1}

Table 2. Fitting band positions of glucose in comparison with experimental band positions at room temperature

Fitting positions of glucose[a]	Experimental positions[b]	Experimental positions[c]
840	840	837
920	917	915
989	995	994
1011		1000
		1014
		1023
1045	1045	1050
1067		1057sh
1085	1078	1078
1108	1105	1103
		1111
		1117sh
1126		1128sh
1166	1146	1149
1203	1202	1203
1228	1222	1224
1250		
1278	1275	1272
1301	1295	1282
		1298
1334		1331
	1340	1339
1351		1345sh
1380	1375	1381
1419	1407	1407
		1427
	1440	1447
1475	1460	1459
2874	2885	
2891	2898	
2915	2920	
2944	2947	
2963		
3138	3100	
3305.758		
3372		
3430.893		

Table 2. (continued)

Fitting positions of glucose[a]	Experimental positions[b]	Experimental positions[c]
3492.735	3500	

[a.] this work

[b.] From Ref. 32

c. From Ref. 25

Table 3. Fitting band positions of cellobiose in comparison with experimental band positions at room temperature

Fitting positions[a]	Experimental positions[b]	Experimental positions[c]
1154	1154	
1163	1161	
1173	1168	
1191	1190	
1205	1204	
1212	1211	
	1217	
1223	1223	
1239		
1253	1250	
1261	1260	
1270	1268	
1284	1284	

Table 3 (continued)

Fitting positions[a]	Experimental positions[b]	Experimental positions[c]
1296		
1301	1301	
1309	1309	
1321	1321	
1331	1331	
1338	1338	
1355	1355	
1361	1361	
1380	1380	
1407	1407	
1428	1428	
1455	1455	
1487	1487	
1536		
3045		
3194		3250
3291		3290
3357		3375
3442		3430
3560		

[a.] this work

[b.] From Ref. 34

c. From Ref. 26

Table 4. Fitting band positions of maltose monohydrate in comparison with experimental band positions at room temperature

Fitting positions[a]	Experimental positions[b]	Experimental positions[c]
849	849	845
863		862
		863
879		883
900	899	907
914	907	
		933
944		956
		979
988	991	986
		993
1004	1006	1013
1020	1027	1027
1031	1038	1041
1056	1073	1048
		1063
		1068
		1071
		1078
		1084
1085	1086	1086
1096	1106	1093
		1112
1119	1124	1122
1130	1135	1137
1145	1150	1145
1158		
1179		1176
1207	1207	1196
		1215
		1220
1226	1227	1227
1249	1249	1229
		1261
1276	1273	1271

Table 4 (continued)

Fitting positions[a]	Experimental positions[b]	Experimental positions[c]
1293	1288	1287
		1297
1305	1308	1302
1317	1319	1311
		1325
1328	1328	1331
		1337
1348	1351	1349
1361	1359	1358
		1367
1376	1377	1375
		1377
1389	1390	1388
1405	1400	1390
		1393
		1396
		1403
		1415
		1424
1436	1434	1433
		1434
		1441
		1452

1460	1459	1458
1475		1478
		1482
		1650
2700		
2807		
		2861
		2865
2852		2873
2897		2884
		2911
		2912
2921		2920
2934		2936
		2939
2948		2943
		2955
2974		2958
		3009
3056		3031
3192		
3315		
3379		3384
3451		3464
		3493

	3521
3564	3565
	3569
	3577
	3587
	3597
	3650

[a.] this work

[b.] From Ref. 31

c. From Ref. 35

3.3 Band Position Shift

Spectra at the starting, medium and ending temperatures were first fitted to sense the shift of band positions. The temperature variation of several representative band positions are shown in Figures 8–10. It turns out that most bands in fingerprint region shift subtly (approximately 3 cm^{-1}), while that in OH region shift 9 cm^{-1} in average by subtracting the band positions recorded at the highest available temperature from those recorded at room temperature. Even though the OH region is broad, but the shift of each band is clear enough to provide quantitative information. Also, there are much less bands in this region which won't affect each other heavily. Moreover, the orientation of the hydroxyl groups affect the glycosidic bonds which indicates the importance of hydroxyl groups. This indicates hydroxyl bonds are more temperature dependent and suggests us to fit more spectra at smaller temperature intervals in the OH region.

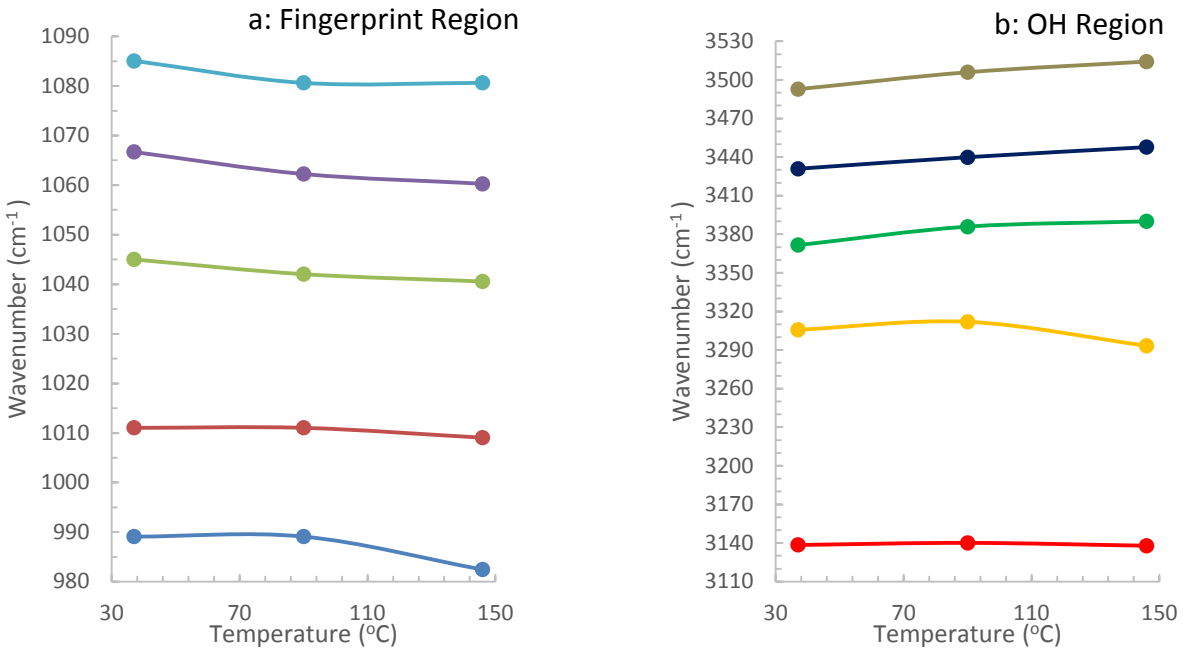

Figure 8. The representative shifts of band positions of glucose from 37°C to 90°C to 146°C at (a) Fingerprint region (b) OH region

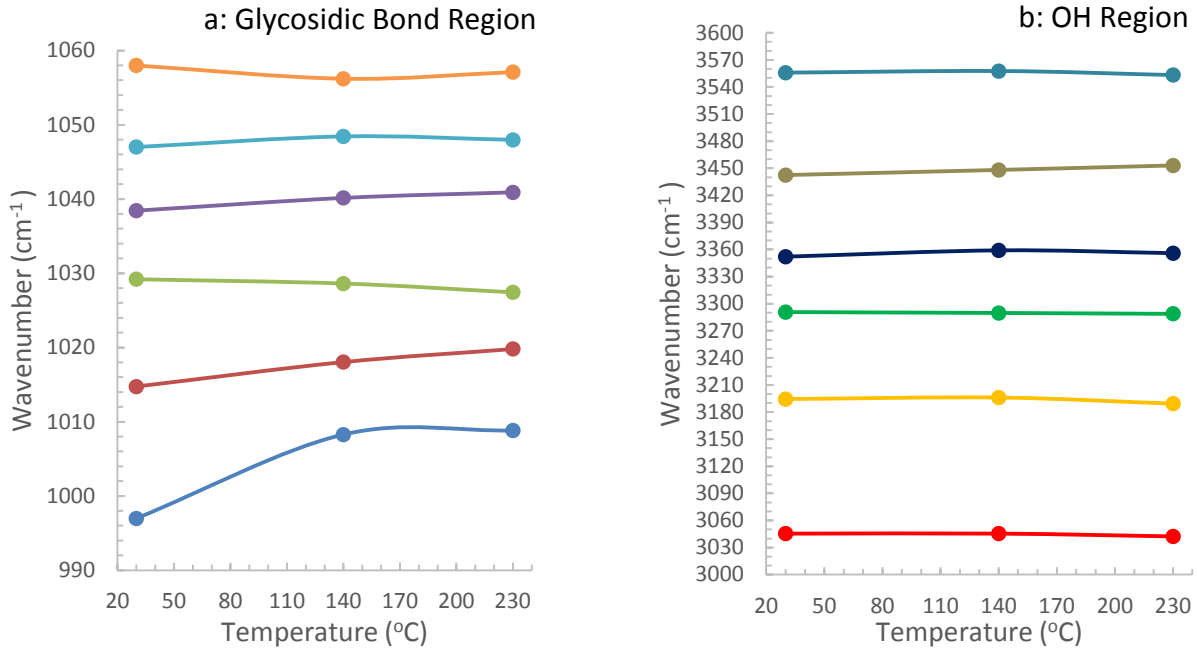

Figure 9. The representative shifts of band positions of cellobiose from 30°C to 140°C to 230°C at (a) Glycosidic bond region (b) OH region

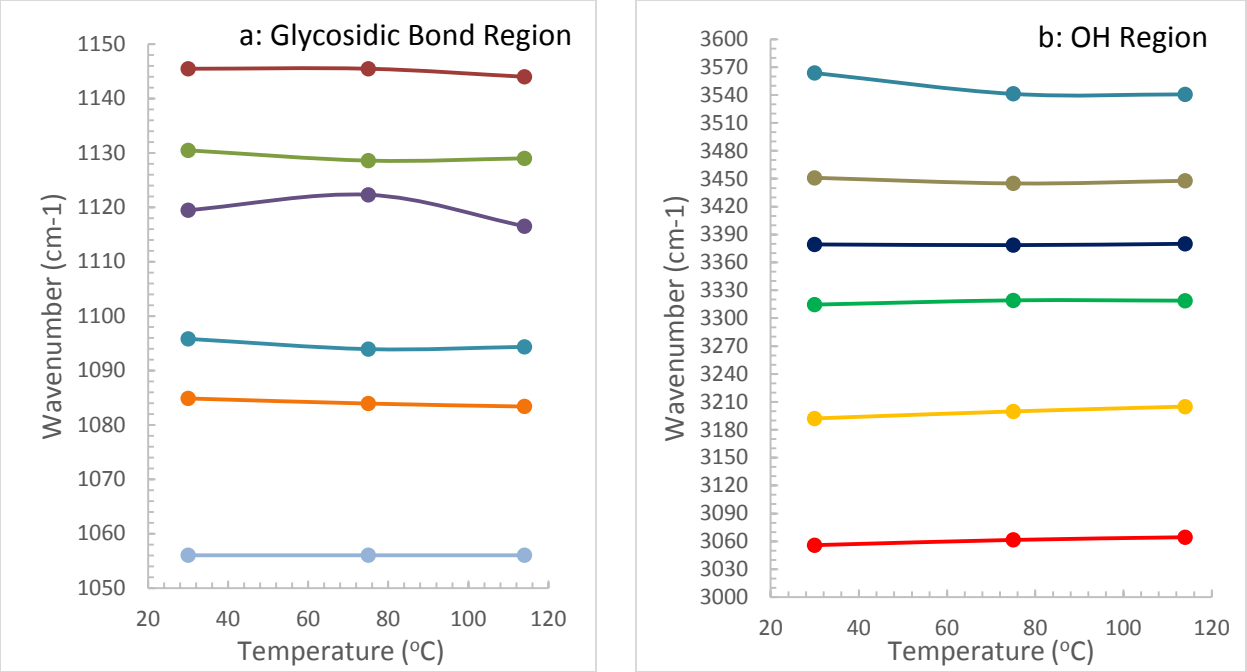

Figure 10. The representative shifts of band positions of maltose from 30°C to 75°C to 114°C at (a) Glycosidic bond region (b) OH region

Figures 11–13 show the band shifts of the hydroxyl bounds of the oligosaccharides at incremental temperatures. More spectra are peak fitted at higher temperatures which the molecular structure is more sensitive to. The error bars are obtained by the standard deviation of the data from duplicate experiments. Most OH groups have a relatively larger shift at the greatest temperature due to its approaching to the melting point, which are not treated as regular shifts. For glucose, the first three OH groups change little (around 4 cm^{-1} from the last second point) which indicates they are not affected by temperature much, while the last three OH groups go through a 15 cm^{-1} average blue shift. For the OH in Figure 11d, the band shifts gradually with the increasing temperature. In Figure 11e, the band blue shifts until 130 °C after which becomes plateau to 140 °C, and shift faster after that, which indicates 140 °C is a threshold for the molecular structure change of OH group. In Figure 11f, the band doesn't change obviously until 70 °C, and it changes slightly

after 90 °C, which means the temperature range between 70 –90 °C affects the molecular structure most. Since glucose is a unit of cellulose polymer, this gives us a clue which bond should be cut first when we make a catalyst for decomposition of cellulose. The disachharides, cellobiose and maltose monohydrate, are then considered as a more complex model to see if they both follow similar shifting trends. The OH group of cellobiose doesn't shift much either in Figure 12a. The reason can be they are the first OH group right next to CH groups which might affect them. OH groups in Figures 12b, c, d shift around 6 cm^{-1} in the end but with large error bars, because they are in the middle of the broad band and our 6 peaks fitting is less than the 7 peaks simulation assignment.[37] The band starting at 3443 cm^{-1} in Figure 12e present a clear blue shift similar to that of glucose confirms it's one of the bands that are most sensitive to temperature change. The last OH group shows a clear 6 cm^{-1} red shift with small error bars at the three highest available temperature. Blue shifts indicate the bond energy of the band decrease and red shifts indicate the opposite change. Similar to glucose, the first three OH groups didn't shift in a large scale for maltose. The only clear blue shift is the band starting at 3444 cm^{-1} in Figure 13e consistent with both glucose and cellobiose with subtle shift of OH groups in Figure 13d and f. Since the paradox of the complexity of the molecular structure and the low melting point of maltose, the shift of it is less clear than that of cellobiose and present more and larger error bars. Additionally, 6 peaks are fitted in our work while 9 peaks are assigned in Maximiliano et al's simulation[35] and moisture absorption on the powder can cause errors.

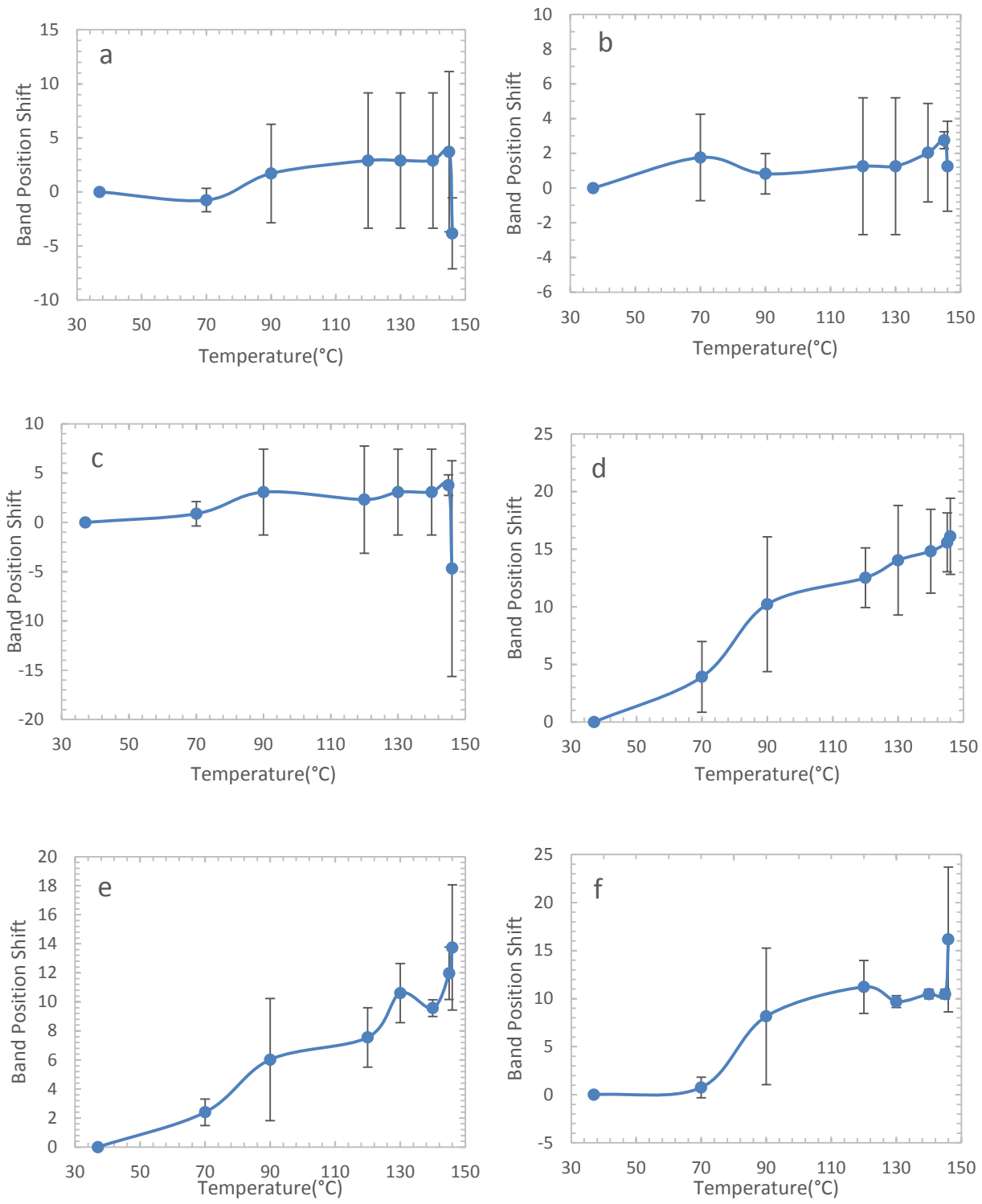

Figure 11. The shifts of band positions of glucose at OH region coresponding to OH groups start at (a) 2963 cm^{-1} (b) 3138 cm^{-1} (c) 3306 cm^{-1} (d) 3372 cm^{-1} (e) 3431 cm^{-1} (f) 3493 cm^{-1}

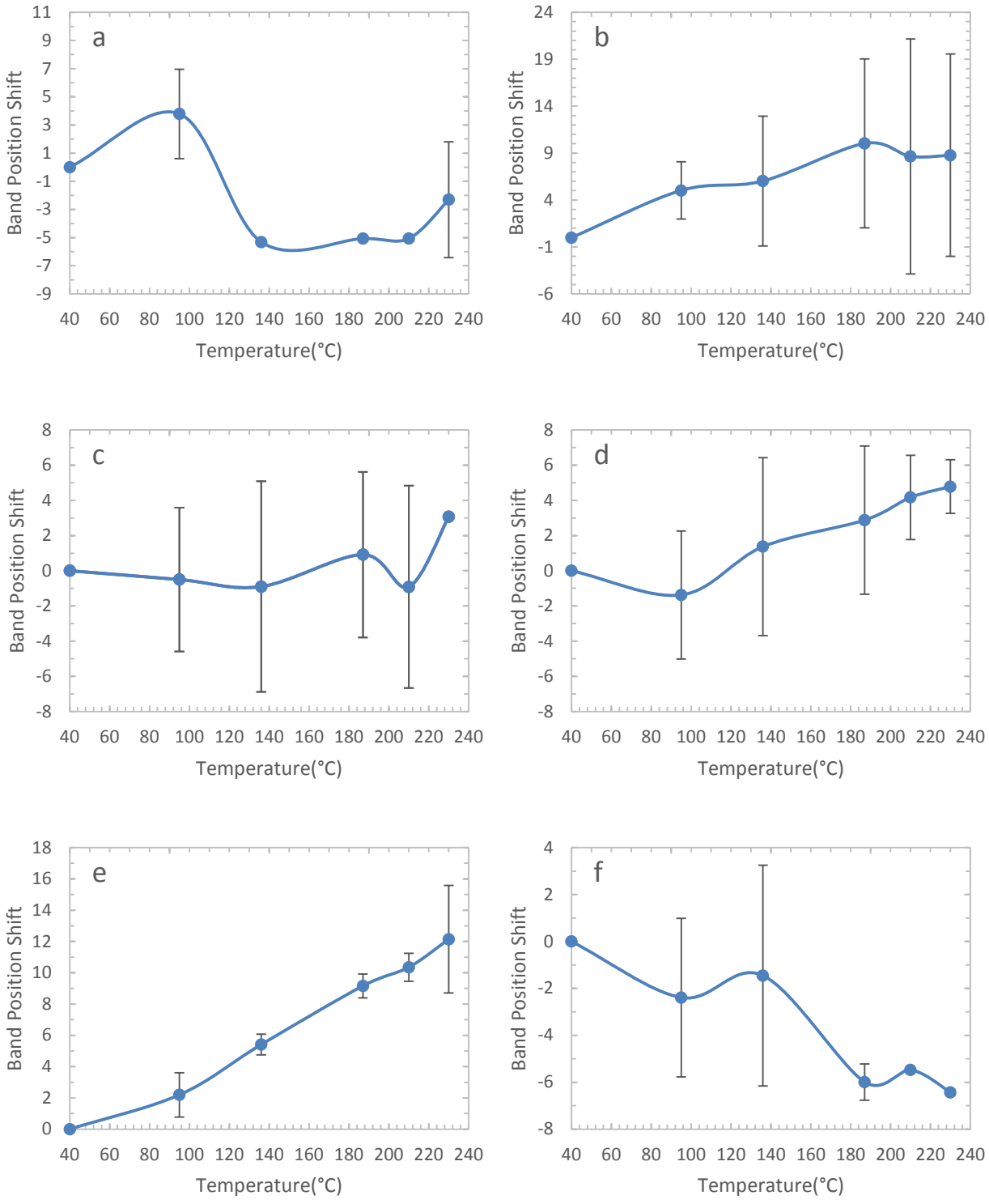

Figure 12. The shifts of band positions of cellobiose at OH region coresponding to OH groups start at (a) 3046 cm^{-1} (b) 3192 cm^{-1} (c) 3292 cm^{-1} (d) 3359 cm^{-1} (e) 3443 cm^{-1} (f) 3560 cm^{-1}

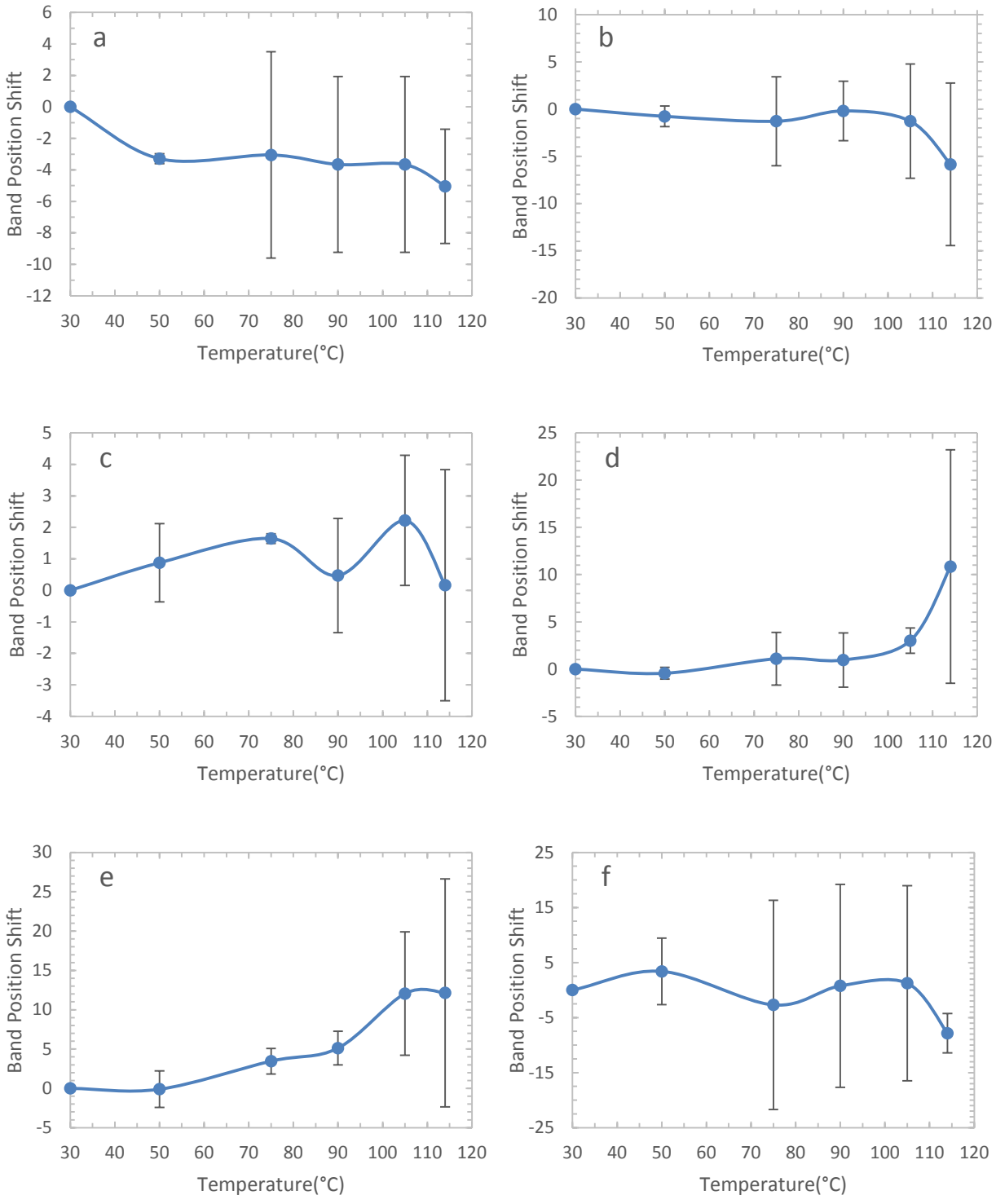

Figure 13. The shifts of band positions of maltose monohydrate at OH region coresponding to OH groups starting at (a) 3045 cm^{-1} (b) 3187 cm^{-1} (c) 3311 cm^{-1} (d) 3378 cm^{-1} (e) 3444 cm^{-1} (f) 3531 cm^{-1}

So we demoisture the maltose and do in–situ IR spectroscopy for it which is shown in Figure 14. From Watanabe's cellulose paper[14], we know the OH band of water is at 1600 – 1700 cm^{-1} and 3000 – 3700 cm^{-1} for cellulose–water mixture. We don't see a continuous decrease of intensity or area at those region in the spectra which means insignificant water effect on the maltose.

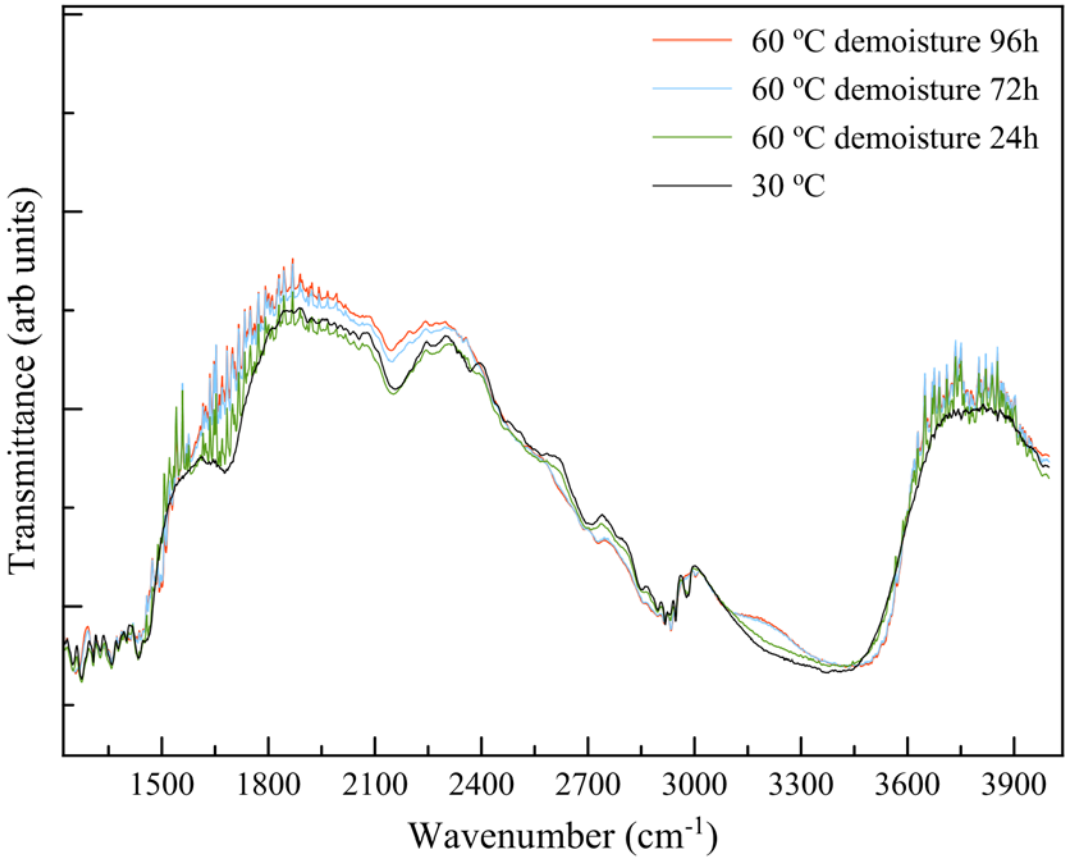

Figure 14. Infrared spectra obtained for maltose under de-watering conditions.

3.4 Simulation Study

The geometry of α–maltose monohydrate was optimized by minimizing the molecular energy and the simulated vibrational spectrum was obtained by calculating the vibrational frequencies and the corresponding intensities. The simulated structure and spectrum show

reasonable concordances with the experimental ones. Since the bands at the fingerprint region overlap extensively and already have relatively comprehensive assignments[2731], we focus on the O–H region simulated spectrum which can assign the peaks to specific chemical groups and increase the reliability of the peak fitting of experimental spectra. Even though the simulated spectrum has deviation from the experimental one, the relative order of the bands at each spectrum should be same. The assignments of the bands are listed in Table 5.

Table 5. Assignments of the simulated spectrum of maltose monohydrate

Mode	Corrected Frequency (cm^{-1})	Frequency (cm^{-1})	Intensity	Assignment
1	3351	3567	442	O7H stretch and water stretch
2	3410	3630	480	O7H stretch and water stretch
3	3487	3713	94	O27H stretch
4	3524	3752	94	O10H stretch
5	3531	3760	69	O24H stretch
6	3564	3794	59	O13H stretch
7	3572	3803	56	O21H stretch
8	3575	3806	49	O2H stretch
9	3591	3823	31	O33H stretch
10	3652	3888	106	water asymmetric stretch

Figure 1 provides the simulated most stable structure of maltose monohydrate with single molecular unit. G. J. Quigley et al [24] show the oxygen in the water molecule (O_{46} in our numbering of the atoms) forms hydrogen bond with H_3 of one molecule unit and H_{25} of another molecule unit, while in my modelling O_{46} interact with H_3 and H_{25} of the same molecule unit. The water molecule forms intermolecular hydrogen bonding with the maltose molecule, which increases the reliability of the simulation. Even though the bond doesn't show in Figure 13, we can tell from the direction of the water O–H bond.

Figure 15 presents the simulated Infrared spectrum compared with the experimental spectrum I got from the FTIR spectrometer which is consistent with the spectra from previous work. [31] Most key peaks associated with specific chemical groups are shown in the simulated spectrum, while the frequency, shape and intensity of the peaks are not in exact agreement with the experimental one. The reason can be there is not enough maltose monohydrate unit for modelling and some contaminant on the material or during obtaining the spectrum with the spectrometer for the experimental spectrum. For frequency, Rebecca A. Jockusch et al [38] scaled the frequencies by 0.9734 which makes a great fit for the simulated spectrum. My linear scale factor is 0.9393 which is calculated by comparing the C–H band at 2917 cm^{-1} in the experimental spectrum with that at 3105 cm^{-1} in the simulated spectrum. The factor decreases the frequencies of C–H band from around 3050 cm^{-1} to 2850 cm^{-1} which is in more accordance with the assignments for C–H bands. It would be better if the peaks at the sides can shrink and shift to the middle of the spectrum. The reason for the deviation of the fingerprint and O–H region of the spectrum is related to the basis set which has different calculation algebra for different chemical groups. The software can increase the peak width to improve the fit between the experimental and simulated spectrum.

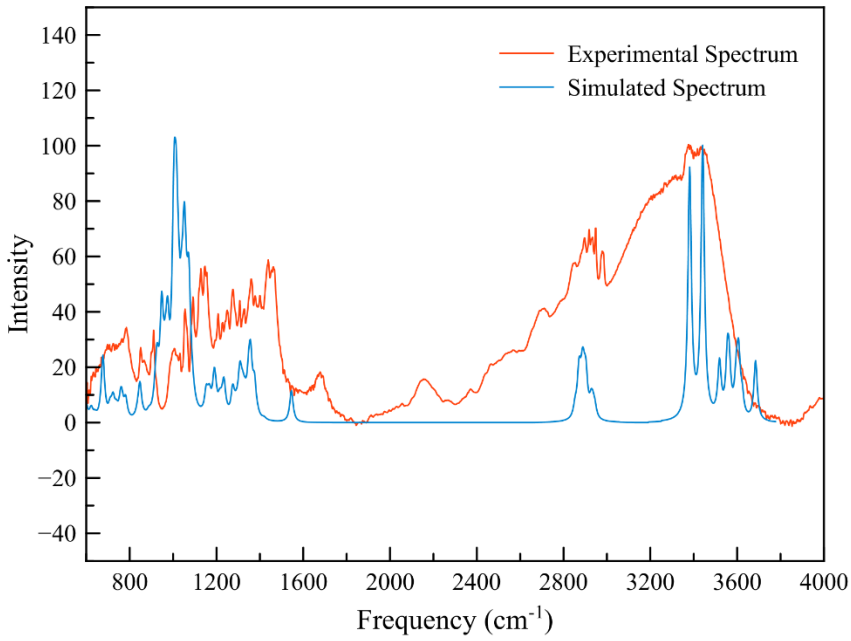

Figure 15. Comparison of scaled experimental and simulated spectra

Table 5 also lists the vibrational mode, corrected frequency (multiplied by scale factor), frequency and intensity of the bands. There are 10 simulated bands in the O–H region which is 1 more than the amount of hydroxyl groups in the molecular unit (water is considered to have 1 hydroxyl group). The reason is O7 and water46 form the peaks at together twice which indicates the strength of the inter–hydrogen bond. The O–H region of the experimental spectrum was peak fitted to 6 bands shown in Figure 7, while table 5 shows the positions of peaks at 3524 and 3531 cm^{-1}, 3564, 3572 and 3575 cm^{-1} are very closed which can overlap to 1 peak and decrease to 7 distinctive peaks. Similar work has done for glucose by my labmate Zhengyang who assigned O–H region for glucose. Because I fit the experimental peaks manually in a homemade software and the spectrum at O–H region is very broad, there can be different shapes and positions of peaks fitting the spectrum. The simulated peaks provide reliable reference to the positions and shapes.

The main vibrational mode of the hydroxyl bonds is O–H stretching with very weak C–O bend. The assignments are obtained by checking the animation of the molecules.

4. Conclusions

Infrared spectra of glucose, cellobiose and maltose were obtained at ramping temperatures until the highest available temperature below the melting point of each material. The spectra are then analyzed by peak fitting to record the band positions of the chemical groups. The temperature variability of the band positions is studied to reveal the respond of specific chemical bonds to elevating temperature treatment. For glucose, the OH groups at 3372 cm^{-1}, 3431 cm^{-1} and 3493 cm^{-1} show the largest temperature dependence. The OH groups at 3443 cm^{-1} and 3560 cm^{-1} of cellobiose present a clear shift at increasing temperatures. However, the OH groups of maltose monohydrate show minor band shifts after temperature treatment. Simulation facilitates the assignment of the OH groups by providing the correspondence of a frequency to an OH group. Analysis of oligosaccharides has the potential to aid the understanding of decomposition of cellulose.

5. Acknowledgements

The author thanks Tom Partington and Douglas White for construction of the in situ Infrared cell and Ravindra Datta for providing the cooling system. Zijian Ma is grateful to N Aaron Deskins on the guidance of computational chemistry work.

6. References

(1) Severian, D. *Polysaccharides: Structural Diversity and Functional Versatility, Second Edition*; CRC Press, 2004.

(2) Tao, L.; Schell, D.; Davis, R.; Tan, E.; Elander, R.; Bratis, A.; Tao, L.; Schell, D.; Davis, R.; Tan, E.; Elander, R.; Bratis, A. **2014**, No. April, 81.

(3) Choi, Y.; Cho, K. W.; Jeong, K.; Jung, S. *Carbohydr. Res.* **2006**, *341* (8), 1020–1028.

(4) Magoń, A.; Pyda, M. *Carbohydr. Res.* **2011**, *346* (16), 2558–2566.

(5) Roos, Y. *Carbohydr. Res.* **1993**, *238* (C), 39–48.

(6) Sharma, P. R.; Varma, A. J. *Carbohydr. Polym.* **2014**, *114*, 339–343.

(7) Hernández-Segura, G. O.; Campos, M.; Costas, M.; Torres, L. A. *J. Chem. Thermodyn.* **2009**, *41* (1), 17–20.

(8) Pinto, S. S.; Diogo, H. P.; Nunes, T. G.; Moura Ramos, J. J. *Carbohydr. Res.* **2010**, *345* (12), 1802–1807.

(9) Shimpi, S.; Chauhan, B.; Shimpi, P. *Acta Pharm.* **2005**, *55* (2), 139–156.

(10) Boutin, O.; Ferrer, M.; Lédé, J. *Chem. Eng. Sci.* **2002**, *57* (1), 15–25.

(11) Watanabe, A.; Morita, S.; Ozaki, Y. *Biomacromolecules* **2007**, *8* (9), 2969–2975.

(12) Lőrinczy, D. *The Nature of Biological Systems as Revealed by Thermal Methods*; 2004.

(13) Lide, D. R. *CRC Press*.

(14) Watanabe, A.; Morita, S.; Kokot, S.; Matsubara, M.; Fukai, K.; Ozaki, Y. *J. Mol. Struct.* **2006**, *799* (1–3), 102–110.

(15) Schreder, B.; Materny, A.; Kiefer, W.; Bacher, G.; Forchel, A.; Landwehr, G. *J. Raman Spectrosc.* **2000**, *31* (11), 995–1003.

(16) Watanabe, A.; Morita, S.; Ozaki, Y. *Biomacromolecules* **2007**, *8* (9), 2969–2975.

(17) Seo, J. A.; Kwon, H. J.; Kim, H. K.; Hwang, Y. H. *Carbohydr. Res.* **2008**, *343* (4), 660–667.

(18) Socrates, G. *John Wiley Sons* **2004**.

(19) Lewars, E. G. *Computational Chemistry: Introduction to the Theory and Applications of Molecular and Quantum Mechanics*; 2011.

(20) Functional, I. D.; Initio, A.; Momany, F. a; Willett, J. L. *J. Comput. Chem.* **2000**, *21* (13), 1204–1219.

(21) Novoat, J. J.; Sosa, C. **1995**, 15837–15845.

(22) Strati, G. L.; Willett, J. L.; Momany, F. A. *Carbohydr. Res.* **2002**, *337* (20), 1833–1849.

(23) Momany, F. a; Willett, J. L. *J. Comput. Chem.* **2000**, *21* (13), 1204–1219.

(24) G. J. Quigley, A. Sarko, lb and R. H. M. *J. Am. Chem. Soc.* **1970**.

(25) Henry A. Wells Jr, R. H. A. Journal of Molecular Structure 1990, pp 385–424.

(26) Zhbankov, E. V. K. V. I. E. K. G. Journal of Applied Spectroscopy 1985, pp 551–553.

(27) Carlson, K. P. **1979**.

(28) v. M. Andrianov, R. G. Zhbankov, and V. G. D. *J. Struct. Chem.* **1980**, *21* (December), 320–324.

(29) P.D. Vasko, J. B. and J. L. K. Carbohydrate Research 1972.

(30) John J. Cael, Jack L. Koenig, and J. B. Carbohydrate Research 1973.

(31) Manuel Dauchez, Philippe Lagant, Philippe Derreumaux, G. V. 1991, pp 105–118.

(32) Manuel Dauchez, Derreumaux Philippe, V. G. Computational Chemistry 1992.

(33) Buslov, D. K.; Nikonenko, N. A.; Sushko, N. I.; Zhbankov, R. G. *Spectrochim. Acta Part A* **1999**, *55*, 229–238.

(34) Buslov, D. K.; Nikonenko, N. A.; Sushko, N. I.; Zhbankov, R. G. *Appl. Spectrosc.* **2000**, *54* (11), 1651–1658.

(35) Iramain, M. A.; Davies, L.; Brand??n, S. A. *Carbohydr. Res.* **2016**, *428*, 41–56.

(36) James, D. I.; Maddams, W. F.; Tooke, P. B. *Appl. Spectrosc.* **1987**, *41* (8), 1362–1370.

(37) Xie, H. Bin; Pincu, M.; Brauer, B.; Gerber, R. B.; Bar, I. *Chem. Phys. Lett.* **2011**, *514* (4–6), 284–290.

(38) Jockusch, R. A.; Kroemer, R. T.; Talbot, F. O.; Simons, J. P. *J. Phys. Chem. A* **2003**, *107* (49), 10725–10732.

Chapter II: Parallel Liquefaction and Carbonization of Coffee Waste during Flow through Hydrothermal Treatment

Zijian Ma,[1] Patricia Guerra,[1] Geoffrey A. Tompsett,[1] Paulo C. Mayanga-Torres,[2] Daniel Lachos-Perez,[2] Tânia Forster-Carneiro,[2] and Michael T. Timko[1]

[1]*Department of Chemical Engineering. Worcester Polytechnic Institute, 100 Institute Road, Goddard Hall 123, Worcester MA 01609.*

[2]*Department of Food Engineering, School of Food Eng., University of Campinas (UNICAMP), Rua Monteiro Lobato, n.80; CEP. 13083 -862, Campinas- SP, Brazil.*

Abstract

Two types of coffee waste products, green coffee beans powder and defatted cake and their hydrolysis residues, were subjected to subcritical water hydrolysis (SWH) under flow conditions at various temperatures (150, 175, 200 and 250 ºC). We characterized the raw and hydrothermal treated solid residues using elemental analysis (EA), thermogravimetric analysis (TGA), Fourier-Transform Infrared (FT-IR) spectroscopy, and Raman spectroscopy to monitor extraction of lipids, hydrolysis of carbohydrates, and carbonization of the residual solids. FTIR spectroscopy indicated that carbohydrates, chlorogenic acid and lipid content decreased during hydrothermal treatment. However, semi-quantitative analysis of the FTIR spectra indicate that sugar acids accumulate during treatment, either because of oxidization of saccharides at solid state or levulinic acid and formic acid bound to the surface of saccharides. In parallel, Raman spectra confirmed FTIR analysis indicating removal of carbohydrates, chlorogenic acid and lipid. Furthermore, Raman spectroscopy revealed that the material undergoes extensive carbonization to form a hydrothermal char product, evidenced by the appearance and growth of peaks characteristic of amorphous carbon. Quantification of TGA indicated the removal of semi-volatile coffee components. Surprisingly, carbohydrates still remain 40% and only 18% biochar are formed in the residue treated at the highest temperature (i.e. 250 °C). Considering Raman spectroscopy is a surface

technique, we suggest that carbonization occurs at the surface. The resulting surface biochar shell limits the access of carbohydrates to solvents explaining certain amount of carbohydrates retention. This explanation suggests low efficiency, consistent with the low total reducing sugar yield in the hydrolyzate (maximum to 9%) as reported by UNICAMP. The combination of elemental, thermal, and spectroscopic analysis techniques provides a powerful technique to understand hydrothermal processing by studying the composition of waste biomass and hydrothermal residues.

Keywords: Coffee bean residue, Waste-to-Energy, Raman spectroscopy, Infrared spectroscopy, Subcritical Water Hydrolysis, Thermal Analysis.

1. Introduction

Food waste is a significant problem in the world, with one third of food intended for human consumption ending as a waste, and the United Nations reporting an estimated 1.3 billion tonnes of food waste per year [1]. Regional data describe a similar situation, with an estimated 90 million tonnes of waste generated from food and beverage production across the EU-27 in 2010 alone [2]. The United States Department of Agriculture estimates that the U.S. wasted 60 million tonnes of food, at an estimated cost of $161.6 billion (U.S.) at consumer prices and the equivalent of 1,249 calories per capita per day [3]. Aside from economic loss, the vast quantity of waste poses huge ethical and efficiency problem, which must be addressed as part of the solution to reducing the estimated 805 million people who went chronically under nourished from 2012-2014 [4].

Multiple, complementary mechanisms that span the entire food production supply chain will be required to reduce global food waste [5]. Because they maximize human benefits, avoidance and donation are the preferred methods of managing food waste [6]. Waste-to-energy technologies can be appropriate for valorization of food waste that has already been generated, cannot be donated, does not have favorable properties to be used as a soil treatment, and that would otherwise

burden landfill management [7]. Valorization of food waste to refined fuels, chemicals, or materials may be preferred in many instances as these products are more valuable than energy in the form of heat or gaseous fuels [8].

Waste-to-energy technologies may be particularly suited to valorization of factory waste food streams as these streams are already available as a concentrated resource. Coffee processing waste is a particularly interesting candidate for waste-to-energy because it is generated in large quantities and its typical acidity limits its use as a soil amendment. Moreover, coffee waste contains abundant valuable organic compounds including lipids, phenols and polyphenols, and chlorogenic acid, compounds valued as a nutraceutical [9-10]. For bioenergy production, Battista, et al. [11] recently reported on the optimization of biogas production from coffee waste; Yun et al. [12] described conversion of coffee waste into mesoporous carbons; and Ngo et al. [13] reported fast pyrolysis of mixed streams of coffee waste and hardwood.

Subcritical water, defined as water held at temperatures between 100 °C and its critical point at 374 °C and at pressures great enough to remain in the liquid phase, holds particular promise for valorization of wet or moist food streams [14]. Subcritical water has been used as a sustainable solvent for the conversion of wet biomass into fermentable sugars, as a pretreatment prior to enzymatic hydrolysis, and for carbonization to high value solids [15-18]. Lachos-Peréz and coworkers [19] subjected sugarcane bagasse to a flow-through subcritical water treatment (100, 150, 200 and to 250 °C and pressures from 5, 10 and 15 MPa) to extract reducing sugars for fermentation. Prado et al. [18] studied hydrolysis kinetics in subcritical water conditions for coconut husks, grape seeds, and palm fiber, obtaining sugar yields ranging from 6.4 to 11.9 g/100 g of raw material. Zhu et al. [20] studied subcritical water at temperatures up to 320 °C to extract sugars and volatile fatty acids from cornstalks.

Flow-through processing of coffee waste has potential to maximize the extraction of semi-volatile organic compounds and sugars from the coffee waste [21]. A solid residue, which can be an appreciable fraction of the original feed material [19], is still obtained following flow-through subcritical water treatment of coffee wastes. Viewing the biorefinery as a system, the hydrolysis conditions must be optimized to obtain the highest value overall distribution of products, and this includes valorization of the residual carbonized solid. However, the carbonized coffee waste has not been characterized previously, nor have the response of coffee wastes subjected to flow-through hydrothermal processing been investigated. Careful characterization of the carbonized coffee waste is necessary to identify conditions that simultaneously maximize the extraction of valuable organic compounds and the value of the carbonized solid, which can have many valuable applications [22]. The objective of this work was to study the extraction and carbonization response of coffee waste residues to flow-through subcritical water hydrolysis using a combination of spectroscopic, thermal, and elemental analysis techniques. This work provides the basis for understanding and designing flow-through subcritical water processes to valorize factory coffee wastes.

2. Materials and Methods

2.1 Raw and Processed Materials

Two sorts of coffee bean waste products, waste powder and defatted cake, and their hydrothermal treated residues were obtained by the University of Campinas, Brazil from Cooxupé (Regional Cooperative of Coffee Growers, Guaxupé Ltda). Green coffee bean waste powder is generated by mechanically abrasive processes, either by friction during transportation or during

quality control, where the grains pass through sieves and qualifying mats that also cause friction between the grains. Defatted coffee cake is produced after separation of low quality beans during the quality control process. Green coffee oil is extracted from the rejected beans using a cold pressing process. The residue of the cold pressing process is the defatted cake which consists of "oil-free" coffee bean bran. Prior to use, the samples were in a freezer stored in a freezer at −18 °C. A knife mill (Marconi, model MA 340, Piracicaba, Brazil) equipped with a 1 mm sieve was used for size reduction before samples were subjected to hydrothermal treatment. Figure 1 provides digital photographs of the green coffee powder and defatted cake. Carbon-hydrogen-nitrogen elemental analysis was performed for both feeds; oxygen was determined by difference. Table 1 summarizes the results.

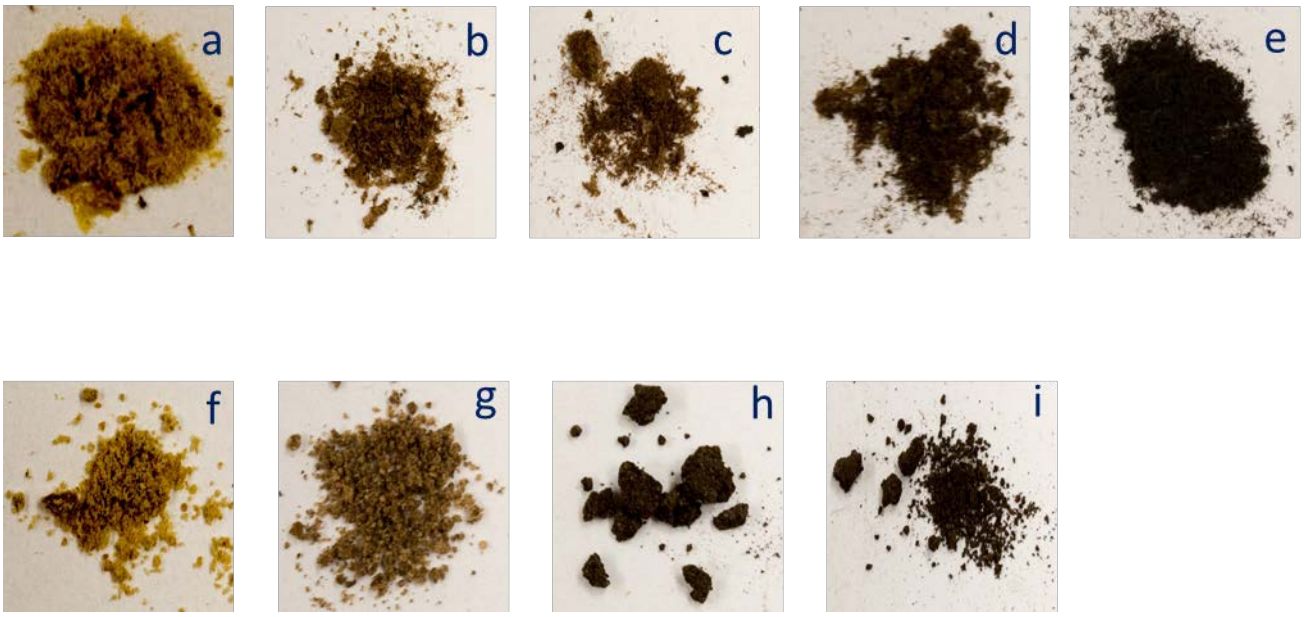

Figure 1. (a) Green coffee powder and its hydrothermal treatment products obtained at: (b) 150°C, (c) 175°C, (d) 200°C and (e) 250°C; (f) deffated cake and its hydrothermal treatment products obtained at: (g) 150°C, (h) 175°C, (i) 200°C

Table 1. Elemental analysis data for coffee wastes.

Sample	Carbon (wt%)	Hydrogen (wt%)	Nitrogen (wt%)	Oxygen (*) (wt%)
green powder	45.2 ± 0.2	6.20 ± 0.4	1.62 ± 0.02	47.0
defatted cake	44.5 ± 0.2	6.90 ± 0.1	2.68 ± 0.05	46.0

* Oxygen content determined by difference.

2.2 Subcritical Hydrothermal Treatment

Hydrothermal treatment of the two coffee wastes has been described elsewhere in detail and only the most relevant details are provided here [19]. The two raw materials were hydrolyzed by subcritical water in a semi-continuous reactor over a range of pre-set temperatures and pressures. A specific amount of material was pressurized with water to remove residual air and then heated to the desired temperature. After temperature stabilization (approximately 13 minutes), water was passed over the packed bed and liquid products collected every 2 min for a total of 36 minutes, at which time the reactor was de-pressurized and cooled to recover the residual solids. The green coffee powder was treated at 150, 175, 200 and 250°C, while the defatted cake at 150, 175, 200°C, both at 22.5 MPa. Figure 1 provides digital photographs of the treated residues.

2.3 Elemental Analysis

Carbon and nitrogen content of the feed and treated samples after hydrothermal treatment were determined using an elemental analyzer Flash model 2000 (Thermo Fisher Scientific Inc.). For the feed samples, hydrogen content was determined in addition to carbon and nitrogen so that

the oxygen content could be determined by difference on a dry and ash free basis. Uncertainties were obtained by analysis of multiple samples and by instrument measurement performance for several standards.

2.4 Spectroscopic Analysis

Infrared spectra were obtained using a Bruker Vertex 70 FTIR spectrometer with a La-DTGS detector at room temperature. Dry powder samples were placed on a Specac diamond ATR cell and spectra collected at 4 cm^{-1} resolution, with 512 scans taken over the 600-4000 cm^{-1} spectral range and then averaged.

Raman spectra of the dried sample powders were obtained using a Horiba XploRa Raman microscope at room temperature. For sample preparation, a small amount of the powder (approximately 100 mg) was placed on a glass slide and the Raman instrument utilized a 785 nm laser line at 25-100 mW, with 1800 grating, and a 100x objective lens. Spectra were obtained using a 5 second scan time and averaging 100 scans. Spectra of 4-5 particles were obtained to examine sample homogeneity. Representative spectra are presented herein.

By virtue of their different selection rules, FTIR and Raman spectroscopy are naturally sensitive to different types of vibrations; IR is most sensitive to vibrations associated with a large change in dipole moment, whereas Raman spectroscopy is most sensitive to vibrations with a large change in polarizability. Therefore, IR is most appropriate for identifying functional groups such as O-H and C=O stretches, while retaining some sensitivity for C-H, C-O, and certain vibrations of C-C and C=C groups. Raman is most appropriate for C-C and C=C stretches and breathing modes, with limited sensitivity to O-H and C=O stretches. By comparison with the spectroscopy literature on biomass materials, we assigned specific chemical groups corresponding to band positions observed both in the IR and Raman spectra. We then used these assignments to study

removal of extracted and hydrolyzed components and the chemical components of the carbonized residue as functions of the carbonization temperature.

2.5 Thermogravimetric Analysis

Thermogravimetric analysis (TGA) of coffee waste and carbonized products were performed in a Netzsch TG 209 F1 Libra. Samples were placed in an alumina crucible and held under a nitrogen flow rate of 20 mL min^{-1}. The samples were heated from 35 °C to 800 °C at a temperature ramp rate of 5°C min^{-1}. Thermogravimetric analysis data were converted into derivative thermogravimetric (DTG) curves using the Netzsch built-in software.

3. Results and Discussion

Two coffee waste products, green coffee powder and defatted cake, and their carbonized residues were characterized using elemental analysis, thermal analysis (TGA), and FTIR and Raman vibrational spectroscopy. For clarity of presentation, we discuss the 2 materials separately. In both cases, we follow an outline the progresses from bulk composition analysis (EA) to molecular functional group identification (FTIR and Raman vibrational spectroscopy) and finally TGA.

3.1 Analysis of Green Coffee Powder and Treated Residues

3.1.1 Elemental Analysis

Our first task was determining the carbon and nitrogen content of the treated green coffee powder samples; Table 2 summarizes the data along with composition data for the feed material. Treatment even at the mildest conditions of 150 °C results in a 7.2 wt% increase in carbon while

the nitrogen content is reduced to nearly half its original value (0.79 wt% compared to 1.62 wt%). At higher treatment temperatures, the carbon content continued to rise, with the largest increases occurring between 200 and 250 °C. Interestingly, nitrogen content either increased modestly or remained constant as the treatment temperature increased from 150 to 250 °C. We take this as evidence of 2 populations of nitrogen-bearing compounds in the green coffee powder, one of which is easily extracted the other of which is thermally stable.

Table 2. Elemental analysis data for green coffee power and treated residues.

Treatment Condition	Carbon (wt %)	Nitrogen (wt %)
feed	45.2 ± 0.2	1.62 ± 0.02
150 °C	52.0 ± 0.2	0.79 ± 0.01
175 °C	52.68 ± 0.08	0.68 ± 0.01
200 °C	55.4 ± 0.4	0.82 ± 0.01
250 °C	62.0 ± 0.5	1.01 ± 0.08

3.1.2 FTIR Spectroscopy

Having analyzed the bulk composition of green coffee powder, we next sought to understand the chemical composition of the extracted, hydrolyzed, and carbonized materials using FTIR spectroscopy. Figure 2 provides infrared spectra of coffee powder and its subsequent hydrothermal carbonization products in the fingerprint region (600-2000 cm^{-1}), and Table 3 lists IR band positions along with literature-based assignments. Initially, the green coffee powder IR spectra indicate the presence of carbohydrates (including starch, identified by its skeletal modes at 670 and 894 cm^{-1}), holocellulose (identified by a dense overlapping of absorption bands in the 1000-1200 cm^{-1} range), lignin (identified by C=C and aromatic ring modes observed at 1508 and

1598 cm^{-1}), lipids (identified in particular by C=O modes associated with triglycerides), and specifically chlorogenic acid (associated with numerous bands, including 1240 and 1374 cm^{-1}). Chlorogenic acid, which is the ester product of caffeic acid and (L)-quinic acid, in particular is a high-value extractable product, marketed for its anti-oxidant properties as a nutraceutical.

Having established peak assignments in the green coffee powder, IR spectroscopy was used to study chemical changes that occur during hydrothermal treatment at different temperatures. First, we review peaks which decrease in intensity during carbonization, data which provides evidence of compound extraction and/or hydrolysis. Peaks associated with fatty acids (initially at 1636 cm^{-1}) decrease in intensity as the carbonization temperature increases, with the most noticeable change occurring between 175 and 200 °C. Similarly, the intensity of the prominent peak attributed to chlorogenic acids and present initially at 1240 cm^{-1} decreases with increasing temperature, with the most of the change occurring from 150 to 200 °C.

Figure 2 shows that bands between 1000 and 1200 cm^{-1}, indicative of the glycosidic bonds present in cellulose, starch, and hemicellulose, become more resolved in the spectra carbonized products. This is particularly evident in the C-O peak initially observed at 1029 cm^{-1}, which becomes increasingly narrow with increasing carbonization temperature. The observation of increased resolution of distinct glycosidic bonds is consistent with removal of hemicellulose during flow-through treatment of the green coffee powder, leaving behind primarily cellulose.

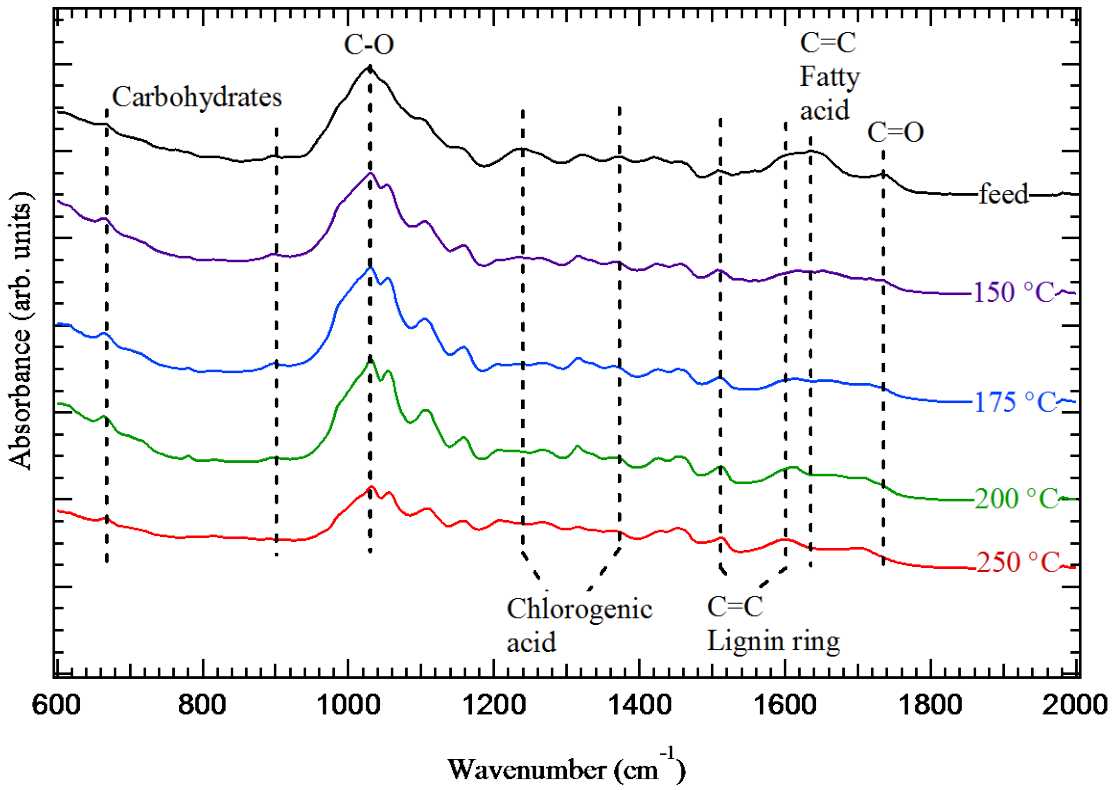

Figure 2. IR spectra of green coffee powder and its hydrothermal treatment products obtained at 150°C, 175°C, 200°C and 250°C in the fingerprint region (600-2000 cm^{-1}).

Table 3. IR band positions and assignments of the spectra at different temperatures for the green coffee powder and its hydrothermal carbonization residues.

Coffee powder (cm^{-1})	**SWH 150°C (cm^{-1})**	**SWH 175°C (cm^{-1})**	**SWH 200°C (cm^{-1})**	**SWH 250°C (cm^{-1})**	**Assignment**	**Reference**
670	668	674	664	664	Skeletal modes (starch)	Reis et al. [23]
	776	780	783	812	modes (starch), α-linked D-galactopyranose units	Reis et al. [23], Ballesteros et al. [24]
894	895	899	894	851	Skeletal modes (starch), β–linked D-mannopyranose units	Reis et al. [23], Ballesteros et al. [24]

Table 3. (continued)

1029	1030	1028	1036	1031	C-O, C-O-H, glycosidic bands from carbohydrates	Reis et al. [23]
	1051	1050	1057	1057	C-O Chlorogenic acids, lignin aromatic C-H deformation	Mishra et al. [25], Agarwal and Atalla [26]
1102	1115	1105	1105	1113	Chlorogenic acids, carbohydrates	Mishra et al. [25], Hineno [27]
1147	1160	1152	1161	1157	Chlorogenic acids, carbohydrates	Mishra et al. [25], Hineno [27]
	1202	1205	1203	1213	carbohydrates	Hineno [27]
1240	1231	1232			Chlorogenic acids	Mishra et al. [25]
	1263	1269	1261	1266	Lignin, aryl ring breathing with C=O	Agarwal and Atalla [26]
1323	1318	1313	1319	1316	Unknown	
	1342	1337	1332	1337	C-O-C ester, lignin O-H bend	Pujol et al. [9], Craig et al. [28]
1374	1368	1366	1367	1361	Chlorogenic acids	Mishra et al. [25]
1422	1424	1424	1430	1430	Unknown	
1457	1456	1448	1457	1451	CH bending of CH_3, Chlorogenic acids, lignin O-CH_3 or CH_2 scissor	Agarwal and Atalla [26]
1508	1509	1504	1512	1509	C=C,	Pujol et al. [9]
1598	1615	1615	1610	1601	C=C, lignin ring C=C	Agarwal and Atalla [26]
1636	1649	1654	1658		C=C, lipids, fatty acids, chlorogenic acids, lignin C=C	Pujol et al. [9], Raba et al. [29], Agrawal and Atalla [26]
1729	1720	1715	1704	1705	C=O, triglycerides or esters	Reis et al. [23], Pujol et al. [9], Raba et al. [29]
2857 2918	2850	2853	2853	2848	C-H aliphatic	Reis et al. [23], Craig et al. [28]
2956	2930	2922	2922	2924	C-H aliphatic	Reis et al. [23], Craig et al. [28]
3322	3337	3337	3334	3339	O-H	Reis et al. [23]

As the intensities of fatty acid, chlorogenic acid, and hemicellulose peaks decrease, other IR peak intensities increase or shift in position. A sharp band, attributable to aromatic breathing modes in lignin and initially present as a shoulder on the fatty acid band observed at 1636 cm^{-1}, increases in prominence with increasing carbonization temperature. The appearance of the lignin

band at 1594 cm^{-1} is directly tied to the disappearance of the broad fatty acid band, consistent with the extraction of the fatty acid band to reveal the lignin. Similarly, persistent bands at around 1250 and 1595 cm^{-1} are indicative of the presence of lignin components after hydrothermal treatment. Interestingly, the band present at 670 cm^{-1} and attributed to starch does not decrease subsequent to treatment. We infer that that this peak is associated either with cellulose or perhaps that a portion of the starch present in the green coffee powder is inaccessible during treatment. The carbonyl band corresponding to chlorogenic acids initially present at 1729 cm^{-1} disappears, and is replaced by a second carbonyl band centered at 1705 cm^{-1} after hydrothermal treatment (see also Figure SI-3 in the Supplementary Material). We attribute the 1705 cm^{-1} band to the presence of carboxylic acid groups on the carbonized residues, consistent with previous literature assignments [30].

3.1.3 Raman spectroscopy

Next, we turned to Raman spectroscopy to track extraction of chlorogenic acid and carbonization of the green coffee powder. Figure 3 contains Raman spectra of the raw coffee bean powder and its hydrothermal solid residues produced at 150, 175, 200 and 250 °C. Table 4 lists Raman band positions and assignments. Figure 3 shows that the Raman spectrum of the green coffee powder contains 9 main bands while only 4 main bands appear in the spectra of treated residues. The bands present at 1656 cm^{-1}, 1596 cm^{-1} and possibly 1120 cm^{-1} in the green coffee powder are attributable to chlorogenic acids and lipids. The band present at 1120 cm^{-1} in particular is associated with a C-H vibration in the cyclohexane ring present in chlorogenic acid. The chlorogenic acid and lipid bands are absent in the carbonized residues treated at 150 °C, indicating their extraction from the solid matrix. The extraction of chlorogenic acid and lipids is in broad agreement with the IR data presented in Figure 2, albeit at a lower temperature. We attribute the

modest extraction temperature discrepancy to the presence of a greater number of overlapping bands in the IR spectra compared to the Raman spectra; the overlapping bands partially obscure the chlorogenic acid band in the IR spectra. With increasing hydrothermal treatment temperature, the intensity of spectral features associated with carbohydrates and initially present at 1092 cm^{-1} diminish. Despite decreasing in intensity, the band present at 1092 cm^{-1} is observed in the spectra of all the materials, consistent with partial retention of carbohydrates in the treated residues. In parallel with the disappearance of carbohydrate features, carbonaceous char features, with broad bands at around 1317, 1435 and 1580 cm^{-1}, begin to appear. These bands are attributable to the graphitic G-band (1580 cm^{-1}) and the disordered D-bands of carbon [31]. Partial overlap between the carbonaceous bands and the residual carbohydrate bands prevents more detailed spectral attributions.

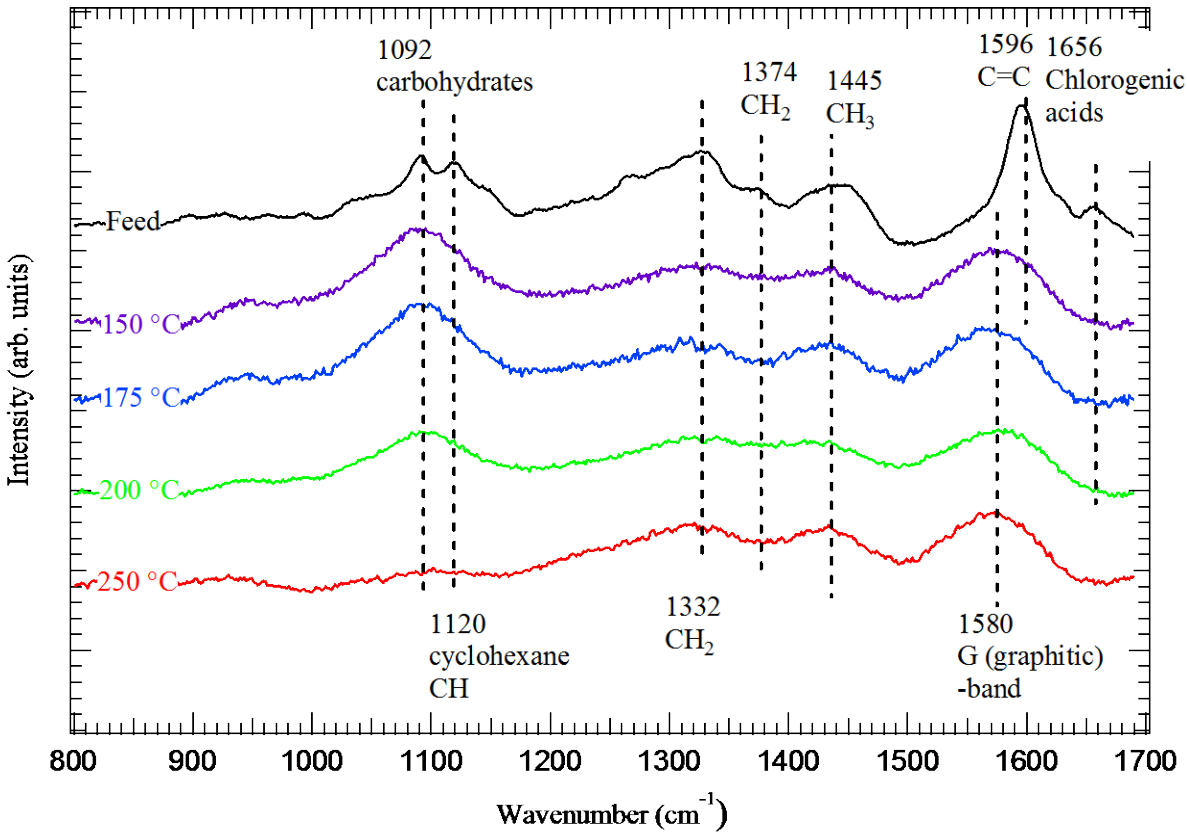

Figure 3. Raman spectra of: raw green coffee bean powder; and solid carbonized residue obtained by hydrothermal treating of green coffee bean powder at: 150 °C, 175 °C, 200 °C and 250 °C.

Table 4. Raman band positions and assignments of the spectra at different temperatures for the green coffee powder and its hydrothermal treatment products

Green Powder (cm^{-1})	SWH 150°C (cm^{-1})	SWH 175°C (cm^{-1})	SWH 200°C (cm^{-1})	SWH 250°C (cm^{-1})	Assignment	Compound	Reference
1656 1596					C=C	Lipids, Polyphenols and phenolic (chlorogenic) acids	Keidel et al. [32] Rubayiza and Meurens [33]
	1580	1580	1580	1580	G-band		Sadezky et al. [31]
1445					CH_3	Roasted coffee, Lipid fraction form arabica and robusta coffee	Rubayiza and Meurens [33]
	1435	1435	1426	1426	D3 band		Sadezky et al. [31]
1374sh 1332 1311sh 1300sh					CH_2	Roasted coffee, Lipid fraction form arabica and robusta coffee	Rubayiza and Meurens [33]
1265					CH deformation	Roasted coffee, Lipid fraction form arabica and robusta coffee	Rubayiza and Meurens. [33]
	1317	1317		1317	D-band		Sadezky et al. [31]
1120					cyclohexane (cyc) CH	Chlorogenic acid	El-Abassy et al. [34]
1092	1096	1096	1096			carbohydrates	
	944	944				Unknown	
576	768	768				Unknown	
375	571	571	571			Unknown	

3.1.4 Thermogravimetric Analysis

FT-IR and Raman spectroscopy analysis of green coffee powder indicated extraction of triglycerides, chlorogenic acids and carbohydrates and appear of biochar at 150 °C. Next, we sought to investigate the samples using TGA to confirm vibrational spectroscopy results and to understand the composition of the residual materials. Figure 4 provides TGA data for green coffee powder as differential thermogravimetric loss (DTG) curves for the feed and for green coffee

powder treated at 150, 175, 200, and 250 °C. From Figure 4, all materials exhibit peaks at temperatures less than 100 °C, readily attributable to sorbed water [35]. The feed material exhibits several prominent peaks in the range 160-240 °C. Consistent with Li et al. [36], we attribute these peaks to evaporation of semi-volatile gases, likely associated with the lipid and chlorogenic acid content of the feed. The feed DTG also exhibits a mass loss peak at 300 °C attributable to hemicellulose and continued mass loss at 400 °C attributable to cellulose [36]. Gradual mass loss at temperatures greater than 400 °C can be associated with lignin content.

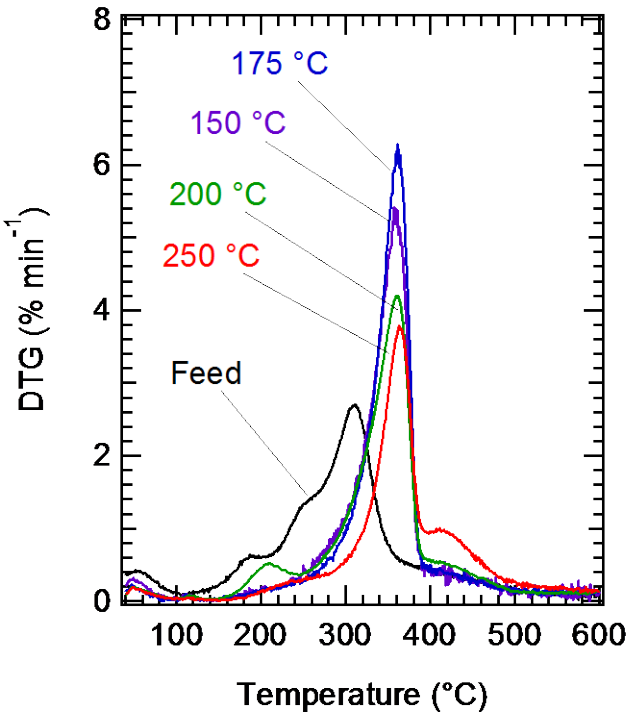

Figure 4. TGA curves (presented as differential thermogravimetric loss, DTG) of green coffee powder and its carbonized residues (treatment temperatures indicated in the plot).

For the treated samples, Figure 4 shows loss of the peaks at 160-240 °C, followed by a gradual shift in composition being dominated by hemicellulose (at approximately 300 °C) to

cellulose (at 360-400 °C). The lignin peak at >400 °C remains constant, up until the sample treated at 250 °C; the sample treated at 250 °C shows a dramatic increase in a peak centered at approximately 400 °C. The peak centered at 400 °C may be associated with carbonization of the green coffee powder during the hydrothermal treatment, though complex thermal behavior of lignin makes ambiguous the attribution from TGA data alone. Interestingly, the sample treated at 200 °C exhibits a DTG mass loss peak centered at 205 °C that is not present in the samples treated at 175 °C or 250 °C. The peak at 205 °C may be associated to the formation of intermediate hydrolysis products that remain insoluble during hydrothermal treatment at 200 °C. Hydrothermal treatment at more severe conditions breaks the intermediates into small, water soluble fragments that are removed under flow conditions and therefore absent from the carbonized residue.

DTG curves are then peak fitted by Gaussian curves to study the quantitative change of the components. Peak fitting of the feed stock is shown in Figure 5 as a representative. The resulting composition of carbohydrates, lignin and water is compared to that measured by the NREL method (Sluiter et al., 2012) shown in Figure 6. It turns out to be reliable with good agreement with the NREL method. Figure 7 presents the fractional composition change after hydrothermal treatment of the coffee powder quantitatively. Most semi-volatile gets removed at the modest temperature, while another type of semi-volatile accumulates at 200 °C and is finally gone. Carbohydrates increase in percentage due to removal of semi-volatile at intermediate temperature and decrease because of decomposition afterwards. Lignin remains unchanged as expected, but 40% of carbohydrates still remain in the residue treated at the highest temperature surprisingly. Moreover, only 18% biochar is formed at the highest temperature contradict with the extensive carbonization feature indicated from Raman spectra in Figure 3. We attributed this to the surface sensitivity of Raman spectroscopy which suggests the char only forms at the surface of the samples. It's

proposed to account for the 40% carbohydrates remain accordingly, because the biochar shell limits accessibility of the carbohydrates.

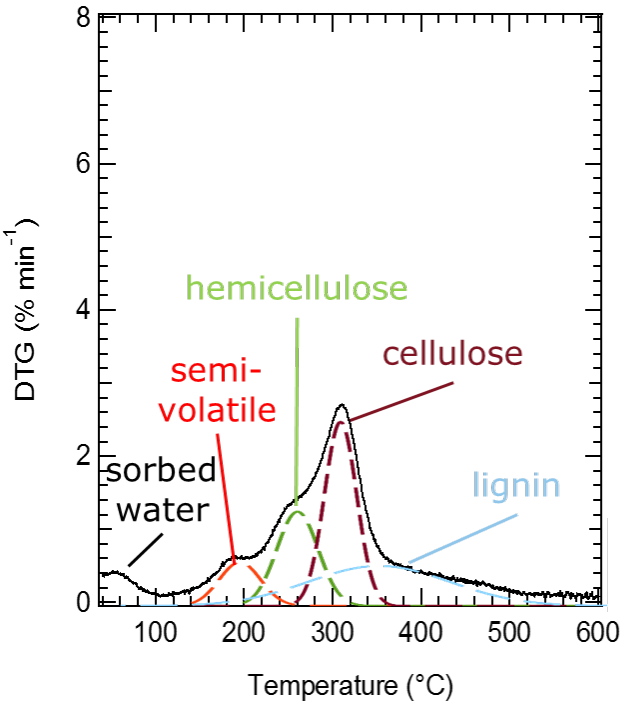

Figure 5. Gaussian peak fitting of DTG curves of green coffee powder as a representative material.

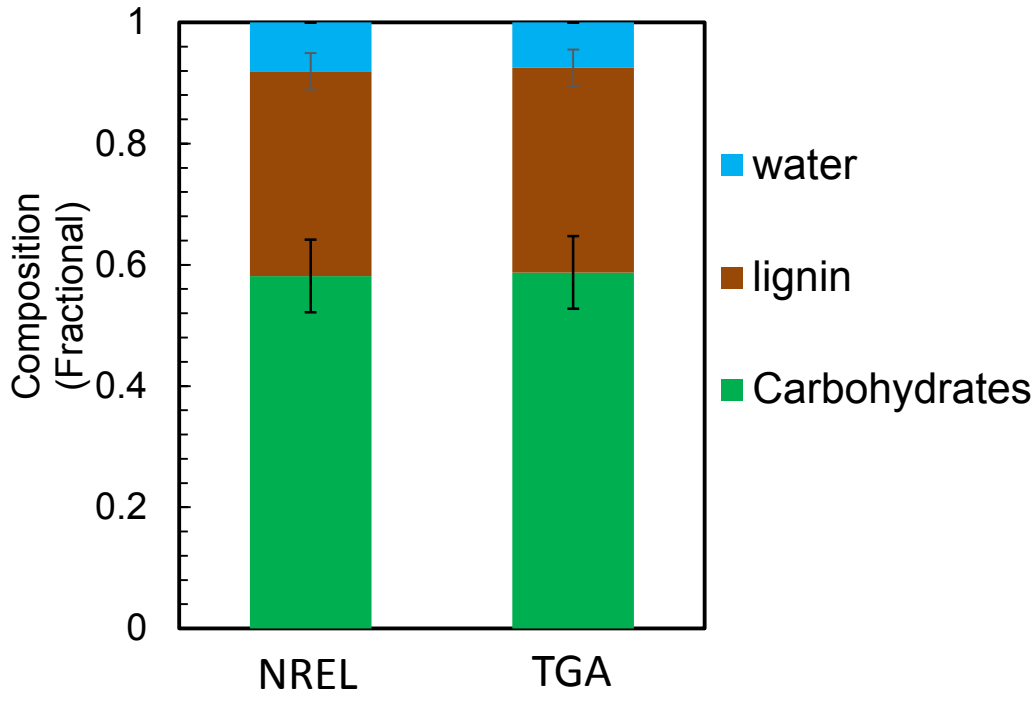

Figure 6. Comparison between methods of DTG peak fitting and NREL on measurement of the composition of the feed stock.

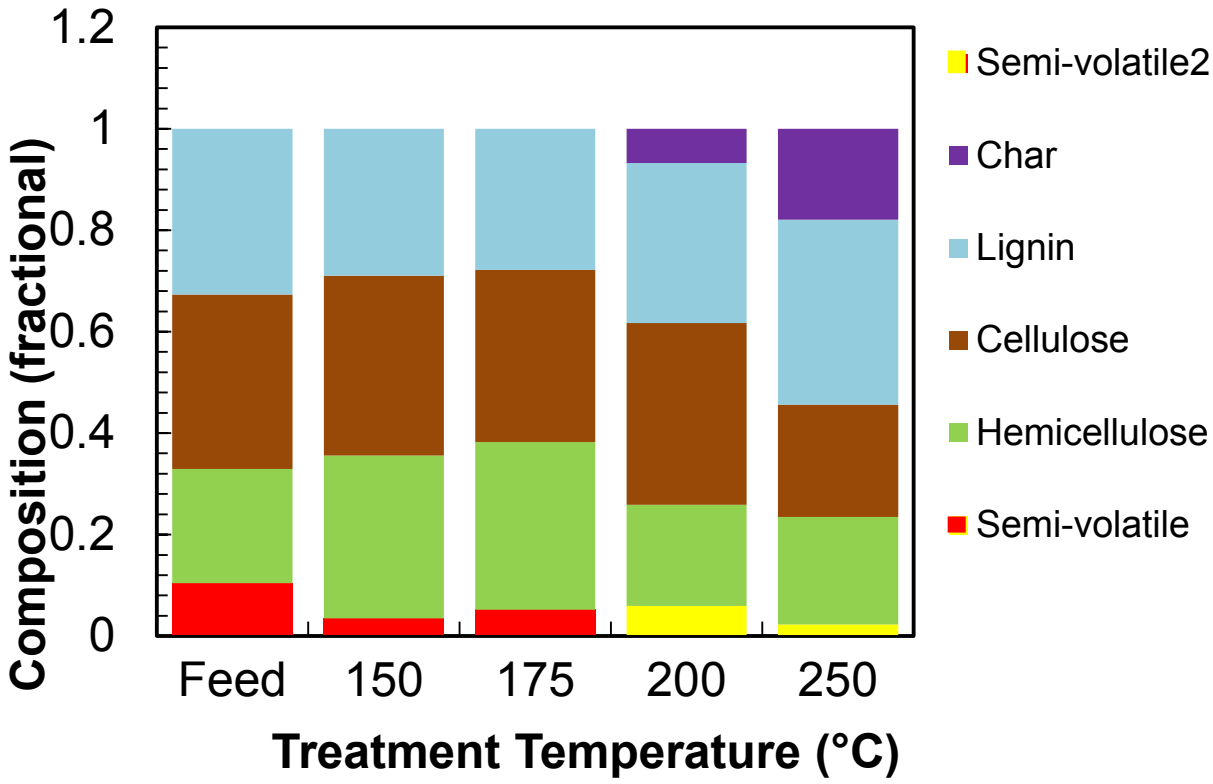

Figure 7. Quantification of the components of coffee powder residues treated at different temperatures by DTG fitting.

3.2 Analysis of Defatted Cake and Treated Residues

3.2.1 Elemental Analysis

Table 5 summarizes CN data for the defatted cake and treated residues. As with the green coffee powder, treatment of defatted cake at 150 °C increases carbon content by approximately 6 wt%

and greatly decreases the nitrogen content (from 2.68 to 0.59 wt%). Treatment at increasing temperatures increases the carbon content up to 56.1 wt%, whereas the nitrogen content is unchanged at temperatures beyond 150 °C.

Table 5. Elemental analysis data for green coffee power and treated residues

Treatment Condition	Carbon (wt %)	Nitrogen (wt%)
feed	44.5 ± 0.2	2.68 ± 0.05
150 °C	50.7 ± 0.3	0.59 ± 0.02
175 °C	56.3 ± 0.2	0.59 ± 0.02
200 °C	56.1 ± 0.4	0.65 ± 0.01

3.2.2 FTIR spectroscopy

Elemental analysis established bulk composition and energy content of the defatted cake and, as with the green coffee powder, we turned to FTIR spectroscopy to identify chemical groups and track the change of the chemicals. Figure 8 provides IR spectra of defatted cake coffee waste product and its carbonized residues. Table 6 lists the associated IR band positions and assignments. Like coffee powder, the defatted cake has an abundance of peaks in the 1000-1200 cm^{-1} range, bands associated with the glycosidic vibrations of carbohydrates. Also similar to coffee powder, the defatted cake has intense bands associated with chlorogenic acid and lipid content, especially at 1053, 1519, and 1642 cm^{-1}. A strong band at appearing at 1740 cm^{-1} is due to the triglyceride content of the cake. Unlike coffee powder, defatted cake lacks prominent lignin bands at 1590 cm^{-1} and 1250 cm^{-1}, indicative of lower lignin content in the defatted cake compared to the powder. Further, unlike coffee powder, the carbohydrate skeletal region (600-900 cm^{-1}) is much more densely populated in the IR spectra of defatted cake, suggesting differences in the carbohydrate content of these two substances. Bands at 1112 and 1150 cm^{-1} may be attributable to

either chlorogenic acid or carbohydrates, though we prefer the latter assignment in accord with the abundance of peaks in the carbohydrate skeletal region.

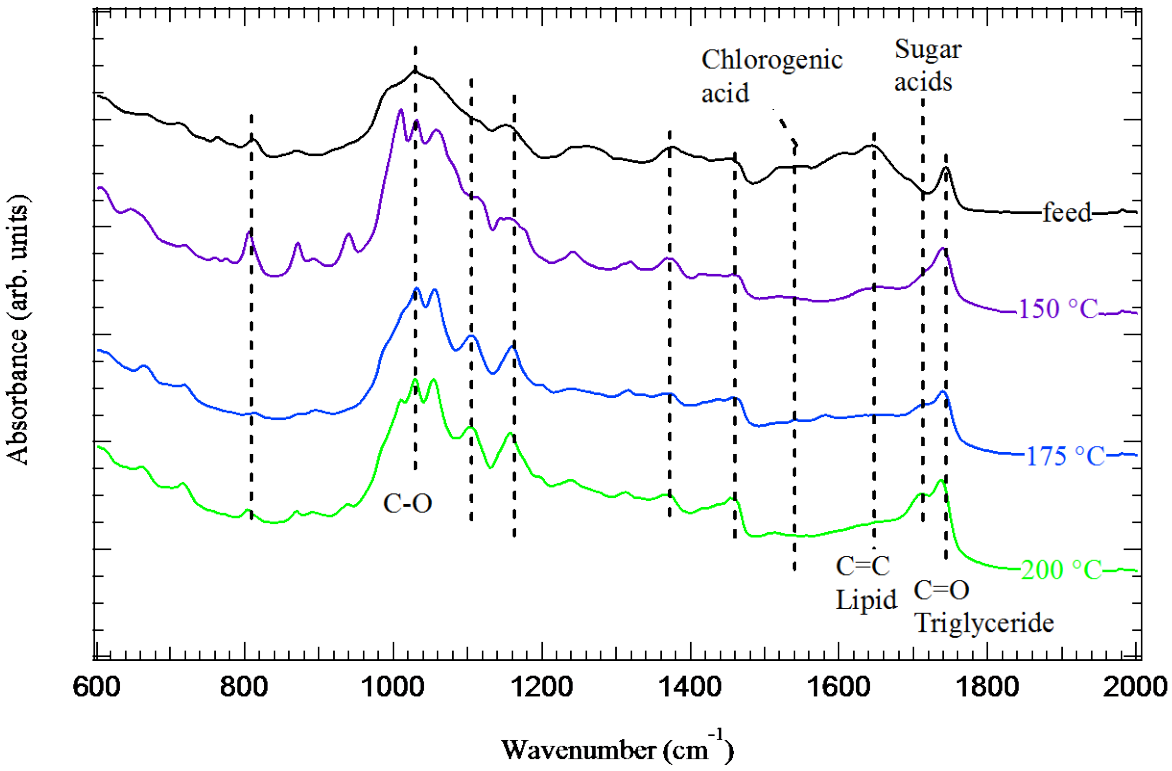

Figure 8. IR spectra of defatted cake and its hydrothermal treatment products formed at 150°C, 175°C, 200°C in the fingerprint region (600-2000 cm^{-1}).

The spectra of treated materials show evidence of both extraction and carbonization. The band at 1640 cm^{-1} attributed to C=C bonds in lipids decreases with increasing treatment temperature raw, indicating the extraction of oils. The band disappears completely between 175 ^{o}C and 200 ^{o}C. Likewise, a broad band centered at approximately 1530 cm^{-1} and possibly associated with chlorogenic acid disappears with increasing treatment temperature. Bands between

1000 and 1200 cm^{-1} become more resolved in the residue, consistent with partial removal of carbohydrates from the defatted cake c. Additionally,

Table 6. IR band positions and assignments of the defatted cake and its carbonized products.

Defatted Cake (cm^{-1})	SWH 150°C (cm^{-1})	SWH 175°C (cm^{-1})	SWH 200°C (cm^{-1})	Assignment	Compound
665	606, 648	664	662	Skeletal modes (carbohydrates)	Reis et al. [23]
714	721	719	718	Skeletal modes (carbohydrates) and/or out-of-plane vibration of cis-di-substituted olefins (lipids)	Reis et al. [23], Ballesteros et al. [24], Raba et al. [29]
763	760			Skeletal modes (carbohydrates)	Reis et al. [23], Ballesteros et al. [24]
	776			Skeletal modes (starch), α-linked D-galactopyranose units	Hineno [27]
811	805	813	809	Skeletal modes (carbohydrates)	Reis et al. [23]
871	871	872	874	Skeletal modes (carbohydrates)	Hineno [27]
	892	893	895	Skeletal modes (carbohydrates)	Hineno [27]
	940		939	Skeletal modes (starch), β–linked D-mannopyranose units	Hineno [27]
997	1010	1012sh	1015	Chlorogenic acids, carbohydrates	Hineno [27]
1027	1030	1032	1031	C-O, C-O-H, glycosidic bands from carbohydrates	Ballesteros et al. [24]
1053	1058	1057	1055	C-O Chlorogenic acids	Mishra et al. [25]
	1112	1105	1108	Chlorogenic acids, carbohydrates	Mishra et al. [25]
1150	1145, 1156	1161	1159	Chlorogenic acids, carbohydrates	Mishra et al. [25]
		1197	1197	Unknown	
1240	1241	1240	1242	Chlorogenic acids	Mishra et al. [25]
1263				Unknown	
	1309, 1320	1317, 1335	1313	CH_2 rocking	
1375	1368	1369	1369	C-O-C ester (lipid)	Pujol et al. [9], Craig et al. [28], Raba et al. [29]
1414	1314	1433	1420	Chlorogenic acids	Mishra et al. [25]
1455	1455	1456	1458	C-H rocking cis-disubstituted olefins	Raba et al. [29]
1519			1515	CH bending of CH3, Chlorogenic acids, lignin	Mishra et al. [25] Pujol et al. [9]
1545		1543		C=C, lignin	Pujol et al. [9], Kang et al. [30]
1607		1582		C=C	

Table 6. (continued)

1642	1632, 1651			C=C, lipids, fatty acids, chlorogenic acids	Pujol et al. [9], Craig et al. [28]
		1715	1712	C=O, triglycerides or esters	Wang and Lim [37], Raba et al. [29]
1745	1740	1743	1737	C=O, aliphatic acids, free fatty acids	Pujol et al. [9], Wang and Lim [37], Raba et al. [29]
2852	2852	2854	2851	C-H aliphatic	Reis et al. [23], Craig et al. [28]
2924	2875	2872sh		C-H aliphatic	
2955	2923	2933	2926	C-H aliphatic	Reis et al. [23], Craig et al. [28]
3009	2956	2959sh	2953sh	C-H aliphatic	
3287	3361	3292	3298sh	O-H, carbohydrates, acids	Reis et al. [23], Craig et al. [28]
	3469	3339	3342	O-H stretch	
	3495			O-H stetch	

chlorogenic acid vibrational features overlap significantly with carbohydrate features in the defatted cake; preferential extraction of chlorogenic acid should improve the resolution of the residual carbohydrate peaks, as we observe in Figure 9. The sharp bands that remain after treatment at 250 °C indicate that significant carbohydrate content remains in the residues, which we attribute to the presence of crystalline cellulose in the defatted cake. Complementary information on carbohydrate recalcitrance to both carbonization and extraction is provided by the persistence of sharp band in the carbohydrate skeletal region from 600-900 cm^{-1}. The intensity of the carbonyl band initially present at 1712 cm^{-1} increases with increasing treatment temperature. We attribute this carbonyl peak to sugar acids, which have formed due to hydrolysis reactions of the carbohydrate content of the defatted cake. It is consistent with low hydrolysate pHs obtained by Torres et al. [38].

3.2.3 Raman spectroscopy

Figure 9 provides Raman spectra of the defatted cake and carbonized solid residues. Table 7 provides The Raman band positions and assignments. Compared to the IR spectra of defatted cake shown in Figure 8, the Raman spectra in Figure 9 are characterized by only a handful of key absorption features. Bands at 1600 and 1627 cm^{-1} are attributable to the presence

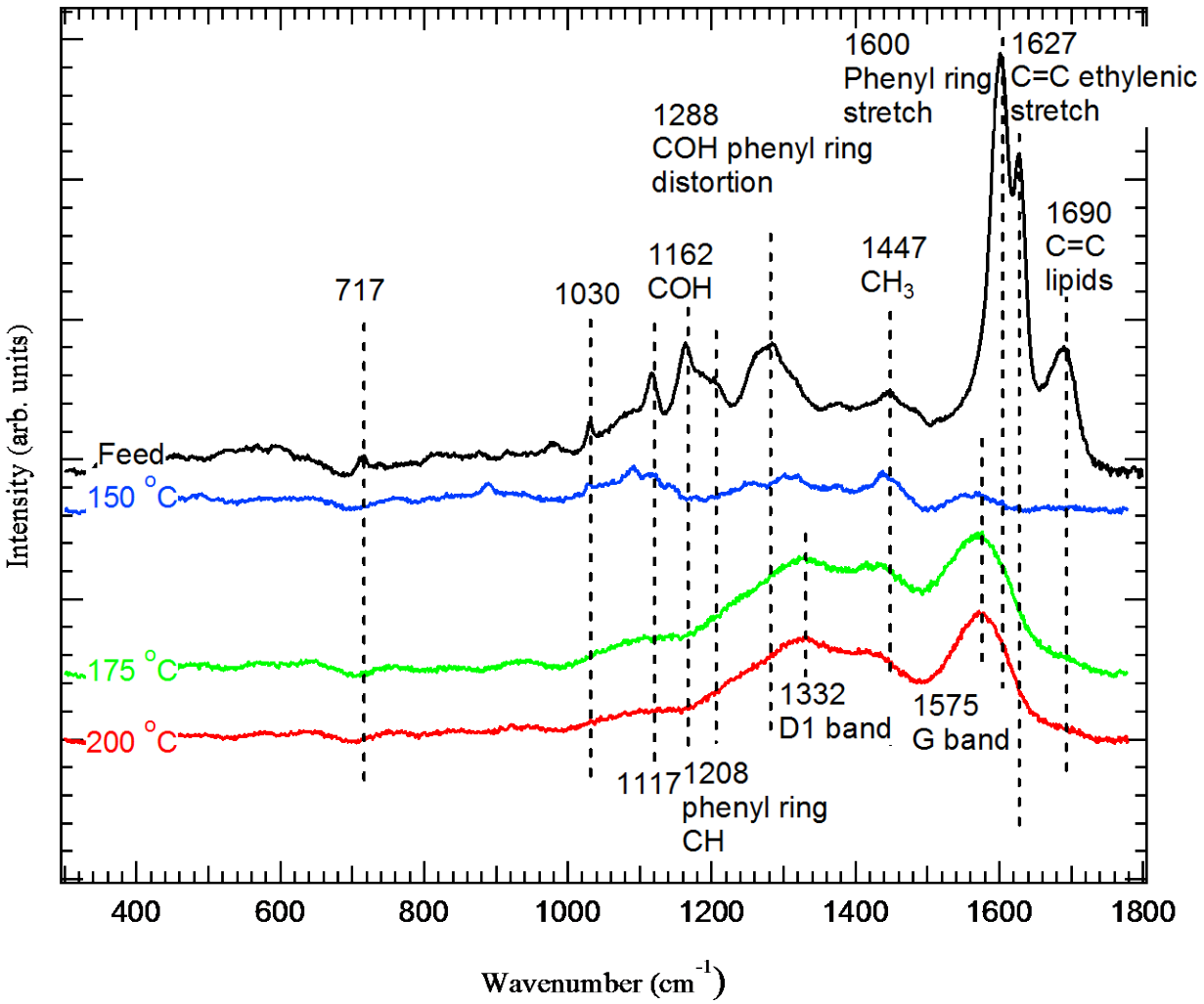

Figure 9. Raman spectra of defatted cake and its hydrothermal treatment products obtained at 150 °C, 175 °C, and 200 °C.

of chlorogenic acids in the defatted cake. These bands are absent in all hydrothermally treated samples, consistent with the chlorogenic acid extraction inferred from the IR spectra. In

comparison with the chlorogenic acid bands, which disappear with hydrothermal treatment, the carbohydrate peaks undergo fewer changes during treatment. The band at 1117 cm^{-1}, assigned to carbohydrates, shifts in position to 1094 cm^{-1} after hydrothermal treatment at 150°C and disappears after treatments at higher temperatures.

While many prominent peaks associated with chlorogenic acid disappear following treatment, two broad new bands, centered at 1332 and 1575 cm^{-1}, appear in the carbonized residues. We identify these new peaks as the D1-band and G-band, associated with disordered

Table 7. Raman band positions and assignments of the defatted cake and its carbonized products.

Defatted Cake (cm^{-1})	SWH 150°C (cm^{-1})	SWH 175°C (cm^{-1})	SWH 200°C (cm^{-1})	Assignment	Compound	Reference
~1660				C=C	lipids	Rubayiza and Meurens [33]
1627				C=C ethylenic stretch	Chlorogenic acid	El-Abassy et al. [34]
	1564	1575	1575	G band, C-C stretching	Ideal graphitic lattice (E2g-symmetry)	Sadezky et al. [31]
1600				Phenyl ring stretch	Chlorogenic acid	El-Abassy et al. [34]
	1438	1436	1436	D3 band	Amorphous carbon	Sadezky et al. [31]
1447				CH_3	Lipid fraction form arabica and robusta coffee	Rubayiza and Meurens [33]
	1313	1332	1332	D1 band	Disordered graphitic lattice (graphene layer edges, A1g symmetry)	Sadezky et al. [31]
1288				COH phenyl ring distortion	Chlorogenic acid	El-Abassy et al. [34]
	1094			Unknown		
1200				phenyl ring CH, bending	Chlorogenic acid	El-Abassy et al. [34]
	939			Unknown		
1162				COH bending	Chlorogenic acid	El-Abassy et al. [34]
	579			Unknown		
1117				Unknown		
	371			Unknown		
1030				Unknown		
717				Unknown		
373				Unknown		

and graphitic carbonaceous materials. The width of the G-band and relative ratio of the D1 and G bands is suggestive of formation of a highly disordered carbonaceous material during hydrothermal treatment. Compared to the IR spectra, the Raman spectra provide a clearer picture of chlorogenic acid extraction by water at 150 °C, in parallel with carbonization occurring at treatment temperatures of 175 °C and greater.

3.2.4 Thermogravimetric Analysis

Figure 10 provides DTG data for defatted cake and the treated samples. Figure 10 shows many superficial similarities compared to Figure 4, especially for the feed material which exhibits peaks for semi-volatiles (a shoulder at about 200 °C), hemicellulose (a prominent peak centered at 300 °C), and cellulose (a distinct peak centered at 360 °C). TGA indicates lower lignin content of the defatted cake compared to the green coffee powder, as suggested by the low DTG values at temperatures greater than 400 °C [36].

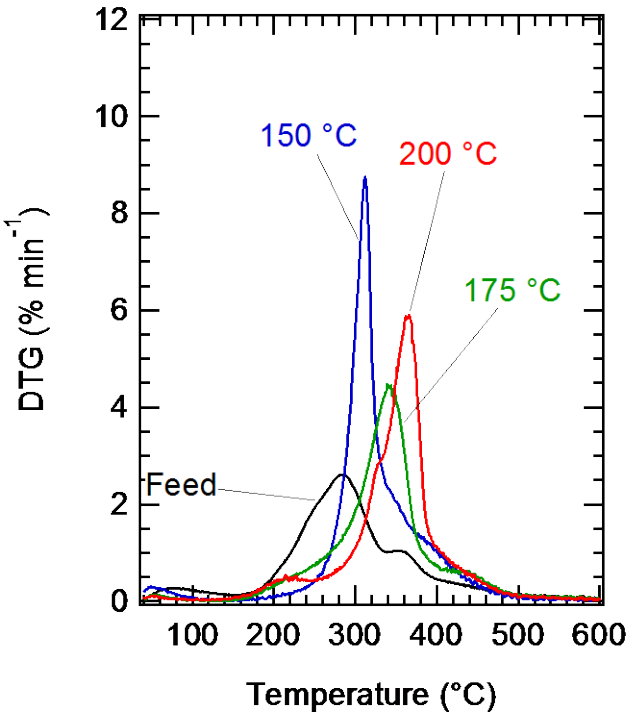

Figure 10. TGA curves (presented as differential thermogravimetric loss, DTG) for defatted cake and its carbonized residues (treatment temperatures indicated in the plot).

Hydrothermal treatment of the defatted cake results in removal of the peak attributed to volatile components at 150 °C followed by a gradual shift from a hemicellulose dominated structure associated with the peak at 300 °C to a cellulose dominated residue associated with the peak at about 380 °C. Carbonization is evident by the steady increase in mass loss at temperatures greater than 400 °C observed for the treated samples. As with the green coffee powder, a new peak centered at 210 °C appears in the sample treated at 200 °C. We attribute the new peak to partial hydrolysis of glycosidic bonds that remain water insoluble. We did not examine treatment temperatures greater than 200 °C for defatted cake, but the green coffee powder data suggest that the new peak observed for the sample treated at 200 °C is an intermediate that would be hydrolyzed fully and extracted under more aggressive hydrothermal treatment conditions.

Similar to quantification of DTG curves of coffee powder, DTG curves of the defatted cake were peak fitted and the change of components are shown in Figure11. Compared to coffee powder, defatted cake present less cellulose than hemicellulose in the raw material. The percentage of lignin increases with temperature. Cellulose increases at 150 °C due to hydrolysis of hemicellulose and decreases at higher temperatures. Change of semi-volatile and char trends similar to those in coffee powder. 24% char were accumulated and 50% carbohydrates remained in the residue treated at 200 °C. Less char formation and more carbohydrates retain in the defatted cake than coffee powder is presumably due to 50 °C lower temperature treatment. The result indicates the surface char structure in consistent with coffee powder analysis.

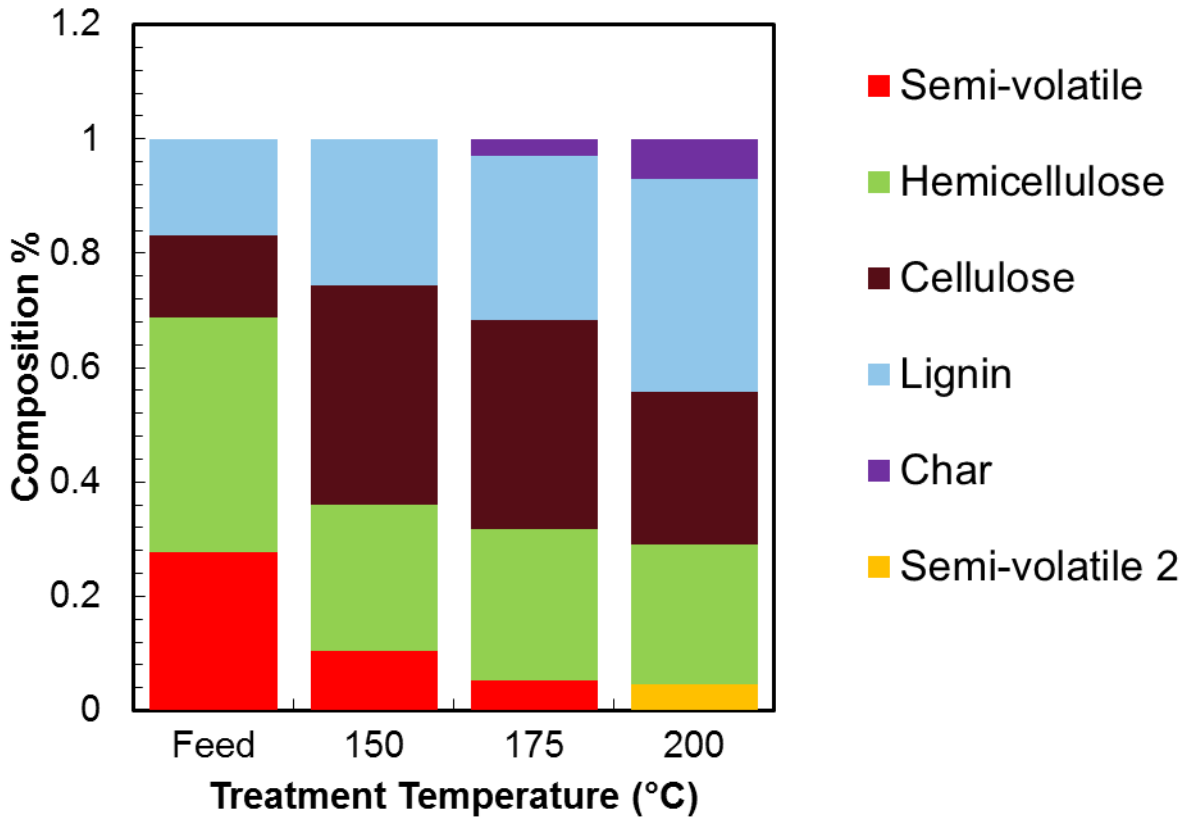

Figure 11. Quantification of the components of defatted cake residues treated at different temperatures by DTG fitting.

In contrast to the carbohydrate content of the coffee wastes, we observed the extraction of chlorogenic acid even at the mildest conditions tested (i.e., 150 °C). The observation of chlorogenic extraction is consistent with SEM images of the carbonized residues that showed that the raw materials were artificially bright due to the abundance of oils in them, whereas carbonized samples did not show evidence of oil content. Similarly, we find lipids extraction to be quantitative at mild conditions. Given the value of these coffee components, our work suggests subcritical water extraction of valuable lipids and acids [9] should be possible without negatively impacting carbohydrate content of the waste.

4. Conclusions

We obtained green coffee powder and defatted cake samples and subjected them to flow-through hydrothermal treatments at temperatures ranging from 150 to 250 °C. For the raw materials vibrational spectroscopy revealed the presence of chlorogenic acids, lipids, carbohydrates, and lignin (in both untreated materials). For treated samples, it suggested extraction of lipids and chlorogenic acid at mild conditions (150 °C) followed by hydrolysis of hemicellulose at intermediate temperatures and possibly carbonization at ≥200 °C. In comparison with the lipids and chlorogenic acids, the carbohydrate content of the coffee waste underwent fewer changes during hydrothermal treatment. Increased spectral resolution in the key regions associated with carbohydrate vibrations was observed and attributed partial removal of carbohydrates, presumably hemicellulose, and retention of others, presumably crystalline cellulose. In parallel with extraction processes, Raman spectroscopy indicated the formation of carbonaceous char species, as evidenced by the appearance of carbonaceous D and G bands after treatment. The D and G bands were broad, indicating that a defect rich underlying carbonaceous structure. Consistent with this Raman spectroscopy, IR spectroscopy identified the presence of aliphatic acids side chains on the carbonized residue. TGA confirmed tentative attributions of vibrational spectroscopy data and provided additional quantitative detail. The results suggested the carbonization happened on the surface, which limits the decomposition of carbohydrates. Previously, Torres et al. [38] studied flow-through liquefaction of coffee powder and defatted cake, reporting hydrolysate composition and pH evolution. Torres et al. [38] observed low carbohydrate content of the coffee wastes and low concentrations of simple sugars in the hydrolysates. Our results are consistent with and accountable for the sugar yields obtained in the hydrolysates.[38] Based on the residual carbohydrate

content observed in the defatted cake, treatment with an acid catalyst might improve the sugar yields obtained in the hydrolysate.

5. Acknowledgements

NSF (award # ECE-1342320) provided partial support for the WPI component of this work. The São Paulo Research Foundation, FAPESP (2011/19817-1), supported UNICAMP's contributions. Cooxupé (Regional Cooperative of Coffee Growers, Guaxupé Ltda) donated coffee residue samples.

6. References

1. Food wastage footprint: Impacts on natural resources, Summary Report. Nations, F. a. A. O. o. t. U., Ed. FAO United Nations: 2013.
2. Final Report-Preparatory Study on Food Waste across EU 27, 2010. Commission, E., Ed. European Commission: 2013.
3. The Estimated Amount, Value, and Calories of Postharvest Food Losses at the Retail and Consumer Levels in the United States. Agriculture, U. S. D. o., Ed. United States Department of Agriculture: 2014.
4. Final Report. Security, C. o. W. F., Ed. Committee on World Food Security: 2014.
5. Parfitt, J.; Barthel, M.; Macnaughton, S., Food waste within food supply chains: quantification and potential for change to 2050. *Philosophical Transactions of the Royal Society B-Biological Sciences* **2010,** *365* (1554), 3065-3081.
6. Girotto, F.; Alibardi, L.; Cossu, R., Food waste generation and industrial uses: A review. *Waste Management* **2015,** *45*, 32-41.
7. Papargyropoulou, E.; Lozano, R.; K. Steinberger, J.; Wright, N.; Ujang, Z. b., The food waste hierarchy as a framework for the management of food surplus and food waste. *Journal of Cleaner Production* **2014,** *76*, 106-115.
8. Kiran, E. U.; Trzcinski, A. P.; Liu, Y., Platform chemical production from food wastes using a biorefinery concept. *Journal of Chemical Technology and Biotechnology* **2015,** *90* (8), 1364-1379.
9. Pujol, D.; Liu, C.; Gominho, J.; Olivella, M. A.; Fiol, N.; Villaescusa, I.; Pereira, H., The chemical composition of exhausted coffee waste. *Industrial Crops and Products* **2013,** *50*, 423-429.
10. Zuorro, A.; Lavecchia, R., Spent coffee grounds as a valuable source of phenolic compounds and bioenergy. *Journal of Cleaner Production* **2012,** *34*, 49-56.
11. Battista, F.; Fino, D.; Mancini, G., Optimization of biogas production from coffee production waste. *Bioresource Technology* **2016,** *200*, 884-890.

12. Yun, Y. S.; Park, M. H.; Hong, S. J.; Lee, M. E.; Park, Y. W.; Jin, H. J., Hierarchically Porous Carbon Nanosheets from Waste Coffee Grounds for Supercapacitors. *Acs Applied Materials & Interfaces* **2015,** *7* (6), 3684-3690.
13. Ngo, T. A.; Kim, J.; Kim, S. S., Fast Pyrolysis of Spent Coffee Waste and Oak Wood Chips in a Micro-tubular Reactor. *Energy Sources Part a-Recovery Utilization and Environmental Effects* **2015,** *37* (11), 1186-1194.
14. Vigano, J.; Machado, A. P. D.; Martinez, J., Sub- and supercritical fluid technology applied to food waste processing. *Journal of Supercritical Fluids* **2015,** *96*, 272-286.
15. Reddy, H. K.; Muppaneni, T.; Sun, Y.; Li, Y.; Ponnusany, S.; Patil, P. D.; Dailey, P.; Schaub, T.; Holguin, F. O.; Dungan, B.; Cooke, P.; Lammers, P.; Voorhies, W.; Lu, X.; Deng, S., Subcritical water extraction of lipids from wet algae for biodiesel production. . *Fuel* **2014,** *133*, 73–81.
16. Mohan, M. B., T.; Goud, V. V., , Hydrolysis of bamboo biomass by subcritical water treatment. *Bioresource technology* **2015,** *191*, 244–252.
17. Prado, J. M.; Lachos-Perez, D.; Forster-Carneiro, T.; Rostagno, M. A., Sub-and supercritical water hydrolysis of agricultural and food industry residues for the production of fermentable sugars: A review. *Food and Bioproducts Processing* **2015**.
18. Prado, J. M.; Forster-Carneiro, T.; Rostagno, M. A.; Follegatti-Romero, L. A.; Maugeri Filho, F.; Meireles, M. A. A., Obtaining sugars from coconut husk, defatted grape seed, and pressed palm fiber by hydrolysis with subcritical water. *The Journal of Supercritical Fluids* **2014,** *89*, 89-98.
19. Lachos-Perez, D.; Martinez-Jimenez, F.; Rezende, C.; Tompsett, G.; Timko, M.; Forster-Carneiro, T., Subcritical water hydrolysis of sugarcane bagasse: An approach on solid residues characterization. *The Journal of Supercritical Fluids* **2016,** *108*, 69-78.
20. Zhu, Z.; Liu, Z.; Zhang, Y.; Li, B.; Lu, H.; Duan, N.; Si, B.; Shen, R.; Lu, J., Recovery of reducing sugars and volatile fatty acids from cornstalk at different hydrothermal treatment severity. *Bioresource Technology* **2016,** *199*, 220-227.
21. Archambault‐Léger, V.; Losordo, Z.; Lynd, L. R., Energy, sugar dilution, and economic analysis of hot water flow‐through pre‐treatment for producing biofuel from sugarcane residues. *Biofuels, Bioproducts and Biorefining* **2015,** *9* (1), 95-108.
22. Libra, J. A.; Ro, K. S.; Kammann, C.; Funke, A.; Berge, N. D.; Neubauer, Y.; Titirici, M.-M.; Fühner, C.; Bens, O.; Kern, J., Hydrothermal carbonization of biomass residuals: a comparative review of the chemistry, processes and applications of wet and dry pyrolysis. *Biofuels* **2011,** *2* (1), 71-106.
23. Reis, N.; Adriana S. Franca; Oliveira, L. S., Quantitative evaluation of multiple adulterants in roasted coffee by Diffuse Reflectance Infrared Fourier Transform Spectroscopy (DRIFTS) and chemometrics. *Talanta* **2013,** *115*, 563–568.
24. Ballesteros, L. F.; Teixeira, J. A.; Mussatto, S. I., Chemical, Functional, and Structural Properties of Spent Coffee Grounds and Coffee Silverskin. *Food Bioprocess Technology* **2014,** *7*, 3493–3503.
25. Mishra, S.; Poonam Tandon; Pinkie J. Eravuchira; Rasha M. El-Abassy; Materny, A., Vibrational spectroscopy and density functional theory analysis of 3-O-caffeoylquinic acid. *Spectrochimica Acta Part A: Molecular and Biomolecular Spectroscopy* **2013,** *104*, 358–367.
26. Agarwal, U. P.; Atalla, R. H., Lignin and Lignans. In *Advances in Chemistry*, Cyril Heitner, D. D., John Schmidt, Ed. CRC Press: 2010.
27. Hineno, M., Infrared spectra and normal vibrations of beta-D-glucopyranose. *Carbohydrate Research* **1977,** *56*, 219-227.
28. Craig, A. P.; Adriana S. Franca; Oliveira, L. S., Discrimination between defective and non-defective roasted coffees by diffuse reflectance infrared Fourier transform spectroscopy. *LWT - Food Science and Technology* **2012,** *47*, 505-511.

29. Raba, D. N.; Poiana, M.-A.; Borozan, A. B.; Stef, M.; Radu, F.; Popa, M.-V., Investigation on Crude and High-Temperature Heated Coffee Oil by ATR-FTIR Spectroscopy along with Antioxidant and Antimicrobial Properties. *PloS one* **2015,** *10* (9), e0138080.
30. Kang, S.; Li, X.; Fan, J.; Chang, J., Characterization of Hydrochars Produced by Hydrothermal Carbonization of Lignin, Cellulose, d-Xylose, and Wood Meal. *Industrial & Engineering Chemistry Research* **2012,** *51* (26), 9023-9031.
31. Sadezky, A.; H. Muckenhuber; H. Grothe; R. Niessner; Poschl, U., Raman microspectroscopy of soot and related carbonaceous materials: Spectral analysis and structural information. *Carbon* **2005,** *43*, 1731–1742.
32. Keidel, A.; David von Stetten; Carla Rodrigues; Cristina Ma ´ Guas; Hilderbrandt, P., Discrimination of Green Arabica and Robusta Coffee Beans by Raman Spectroscopy. *J. Agric. Food Chem.* **2010,** (58), 11187–11192.
33. Rubayiza, A. B.; Meurens, M., Chemical Discrimination of Arabica and Robusta Coffees by Fourier Transform Raman Spectroscopy. *J. Agric. Food Chem.* **2005,** *53*, 4654-4659.
34. El-Abassy, R. M.; Patrice Donfack; Materny, A., Discrimination between Arabica and Robusta green coffee using visible micro Raman spectroscopy and chemometric analysis. *Food Chemistry* **2011,** *126*, 1443–1448.
35. Skreiberg, A.; Skreiberg, Ø.; Sandquist, J.; Sørum, L., TGA and macro-TGA characterisation of biomass fuels and fuel mixtures. *Fuel* **2011,** *90* (6), 2182-2197.
36. Li, X.; Strezov, V.; Kan, T., Energy recovery potential analysis of spent coffee grounds pyrolysis products. *Journal of Analytical and Applied Pyrolysis* **2014,** *110*, 79-87.
37. Wang, N.; Lim, L.-T., Fourier Transform Infrared and Physicochemical Analyses of Roasted Coffee. *J. Agric. Food Chem.* **2012,** *60*, 5446−5453.
38. Torres, P.; Lachos-Perez, D.; forster-Carneiro, T. In *Hidrólise em água subcritica para produçâo de açucares redutores totais a partir do resíduo de pó de café verde*, 10º Congresso sobre Geração Distribuída e Energia no Meio Rural, Universidade de São Paulo – USP – São Paulo, November, 2015; Universidade de São Paulo – USP – São Paulo, 2015.

Chapter III: Structural Characterization of Lignins from Co-solvent Enhanced Lignocellulosic Fractionation of Wood and Biomass Residue

Zijian Ma[1], Geoffrey A. Tompsett[1], Patricia Guerra[1], Charles M. Cai[2], Charles E. Wyman[2] and Michael T. Timko[1,*]

[1]Department of Chemical Engineering. Worcester Polytechnic Institute, 100 Institute Road, Goddard Hall 123, Worcester MA 01609, USA.

[2]Center for Environmental Research and Technology (CE-CERT), Bourns College of Engineering, University of California, Riverside, 1084 Columbia Avenue, Riverside, California 92507 USA.

Abstract

Three wood materials, bagasse, maple wood, poplar wood and their biomass residue obtained from co-solvent enhanced lignocellulosic fractionation treatment were characterized. The bulk composition, crystallinity and surface chemistry were investigated by thermogravimetric analysis (TGA), X-ray Diffraction (XRD) and vibrational spectroscopy (Infrared and Raman spectroscopy). TGA indicates removal of carbohydrates and formation of biochar and ash after CELF treatment. DTG present the components, cellulose, hemicellulose and lignin in the feed stock and remain of cellulose after treatment. XRD and vibrational spectroscopy are consistent with TGA on removal of carbohydrates. Vibrational spectroscopy assigned the vibrational bands and identified chemical groups. Infrared spectroscopy revealed it's more difficult to extract lignin from poplar wood. Retain of carbohydrates in poplar wood is further confirmed by Raman spectroscopy that band of carbohydrates diminished after enzymatic treatment.

Key words: lignin, Raman spectroscopy, infrared spectroscopy, co-solvent fractionation, thermogravimetry, X-ray Diffraction

1. Introduction

Lignocellulosic biomass, composed of cellulose, hemicellulose and lignin, is a promising alternative feedstock for transportation fuels, such as ethanol, which has attracted wide attention in the area of renewable energy. [1, 2] Fermentation or hydrolysis of cellulose and hemicellulose produces ethanol or fuel precursors, and lignin can be depolymerized to phenolic monomers and chemical precursors. [3, 4] Biomass has mainly sources from jute, hemp, cotton and wood pulp?. [5] It exists in the agricultural, herbaceous, and woody residues and energy crops extensively in the nature. [6] The equivalent energy produced by $60 dry biomass/ton and $20 oil/barrel makes biomass competitive from the aspect of resource.[7] Cellulosic ethanol is a promising biofuel from the aspect of green house gas reduction, agriculture yield and energy efficiency. However, the recalcitrance of lignocellulosic biomass, as an alternative renewable source to the first generation sources such as corn starch, limits access of enzymes to cellulose and hemicellulose to convert to valuable products, e.g., glucose, ethanol and etc. [1,6,8] The degree of lignification, the structural heterogeneity, complexity of cell-wall components are considered as contributors to the recalcitrance. [9] Pretreatment is a key process to improve the process and economics by liberating the sugars held in the lignin-carbohydrates hetero-matrix structure.[10] Lignin is insoluble in water and glues carbohydrates together, which partially results in the recalcitrance of biomass. It's employed in broad areas including dyes, synthetic floorings, sequestering, binding, paints and etc. [11] It has to be removed to open the cover of carbohydrates so that they can be efficiently converted to ethanol [5,12]

Several essential improvements have been made to produce cellulosic ethanol including modifying components of lignin to reduce the recalcitrance of biomass, advancement in analytical chemistry and computational modelling and biomass pretreatment that facilitate lignin recovery and catalysis that yield targeted products.[13] In 2007, Chen and Dixon [14] downregulated lignin biosynthesis in alfalfa with antisense-mediation, which is potentially able to reduce or eliminate the necessity of pretreatment. A consortium of hyperthermophilic (growth at 90 °C) archaea was

identified and analyzed for deconstruction of crystalline cellulose using sequence and phylogenetic analysis. [15] Four types of methods, biological, chemical, physical, and thermal processes are mainly used for pretreatment of biomass. [16] Detroy et al. [17] employed a microorganism, Pleurotus ostreatus, to selectively degrade lignin and cellulose with a limitation of slow reaction rate. Ball milling increases the surface area to volume ratio, depolymerizes biomass and hydrolyzes cellulose, but does not improve sugar conversion substantially. [18] Chaogang et al. [19] pressurized hot water through biomass increasing the solubilization of hemicellulose and removal of lignin effectively. Unfortunately, high temperature (220°C) used in this process lead to formation of pacipitates which impede lignin removal.

Charles et al.[20] promoted the yields of hydrocarbon fuel precursor with tetrahydrofuran (THF) as a co-solvent from a representative biomass-- maple wood, which is called Co-solvent Enhanced Lignocellulosic Fractionation (CELF) processing. The reaction is conducted in a continuous batch at 170 °C with 1% sulfuric acid and THF forming an azeotrope with water at 1:1 ratio. They achieved yields of 86% furfural, 21% 5-hydroxymethylfurfural (HMF), 40% levulinic acid (LA) in the liquid phase, over 90% extraction of lignin and highly digestible glucan rich residue, using the CELF process. Later they improved application of metal halides as catalysts directly on lignocellulosic biomass in integration with CELF process, $FeCl_3$ showed the most effective results that the optimal yields of furfural, 5-HMF and LA reach 95%, 51% and 6% respectively. [3] Sets of characterizations of biomass verify the results of experiments and provide clues for the future steps.

SEM images demonstrated the disruption of the fibrous structure of maple wood treated by THF, which indicated maple wood is easier to hydrolyzed with THF as a co-solvent. [20] Long et al.[4] leveraged elemental analysis, FT-IR spectroscopy and etc. to study the effect of catalyst dosage on raw lignin and residual solid of depolymerization, they found the base-catalyst, MgO, can inhibit char formation signinficantly which repolymerize on the pore and surface of the catalyst and decline the catalytic performance. Eva et al.[21] compared the crystallinity of holocellulose, sulphite pulp and kraft pulp, and tried to categorize Iα or Iβ dominant type of cellulose using X-ray diffraction (XRD). Both the fibril structure and fibril aggregation of them turn to be remarkably different, kraft pulp present the highest crystallinity among all the materials. Simulation analysis of lignin in THF-water environment provides insights that lignin is in coil state in the co-solvent

system even it's at low temperature where the co-solvent is immiscible instead of high temperature miscible region. The results suggest CELF processing may work at relatively low temperature.[22]

In this work, we characterized the structural properties and composition of three different raw cellulosic biomass and the corresponding lignin residue after CELF processing treatment. A combination of thermogravimetry, vibrational spectroscopy and X-ray diffraction is used to compare their structures and different reactions to the treatment so that we can understand what happened after treatment from the aspect of lignin residue. Optimally, the characterization can help maximize the yield of valuable products and select a better candidate biomass.

2. Experimental

2.1 Biomass and lignin materials / CELF processing

Three biomass feedstocks were used in the work, namely, poplar wood, maple wood and sugar cane bagasse. These air-dried materials were sourced from NREL. The woods first went through a particle size reduction process, then were loaded into a 1 L Hastelloy Parr® autoclave reactor for pretreatments. An impeller rotating at 200 rpm is used to mix the 5 wt% biomass particles, 0.5 wt% sulfuric acid (Ricca Chemical Company, Arlington, TX) and the 1:1 ratio THF(>99% purity, Fisher Scientific, Pittsburgh, PA)-water solution. The reaction solutions, temperatures, and times for the CELF pretreatment technologies were 150°C 25 min for bagasse, 160°C, 15min for Poplar wood and 160°C, 15min for maple wood.

For the Poplar wood biomass material, Accellerase® 1500 cellulase cocktail (DuPont Industrial Biosciences, Palo Alto, CA) was employed to enzymatic hydrolyze carbohydrates.

2.2 Thermogravimetry

The whole biomass materials and lignin residues were studied using a simultaneous Netzsch TG 209 F1 Libra TGA/DTG analyzer. Around 5 mg sample was finely chopped by a razor for better distribution in the crucible. The experiment was conducted in nitrogen at a flow rate of 20 mL min^{-1} with a temperature range from 35 °C to 800 °C at a rate of 5°C min^{-1}.

2.3 X-ray Diffraction

X-ray diffraction patterns were obtained using a Bruker X-ray diffractometer using CuKα radiation at 37.5 kV and 25 mA. A step size of 0.05° (2θ) was used with 1 second accumulation time. Patterns were obtained over the 2 theta angle of 5-90°. The cellulose crytallinity in the biomass materials was estimated using the peak deconvolution method described by Park et al.[23]

2.4 Infrared Spectroscopy

Infrared spectra were recorded with a Bruker Vertex 70 FTIR spectrometer in the range 600-4000 cm^{-1}. A Specac diamond ATR cell held dry powder biomass samples and lignin residues. The spectra were collected at 4 cm^{-1} resolution using a La-DTGS detector, with 512 scans taken and then averaged.

2.5 Raman Spectroscopy

A Horiba XploRa Raman microscope was used to record Raman spectra of the whole biomass materials and lignin residues. A small amount of the powder (approximately 10 mg) was placed on a glass slide and analyzed using a 785 nm laser operating at 25-100 mW. Spectra were obtained using a grating with 1800 groves mm^{-1} and samples imaged using a 100x objective lens (Olympus). A 5 second scan time was used and spectra were averaged over 100 scans to improve signal to noise. We measured spectra of 4-5 particles for each sample to find a best resolved one.

3. Results and Discussion

Three biomass feedstock materials, bagasse, maple wood and poplar wood, together with their lignin residues from the CELF process, were investigated. In addition enzyme treated poplar wood was compared to CELF extracted lignin residue. These biomass feedstocks and residues were characterized using thermal analysis (TGA), X-ray diffraction, FTIR and Raman spectroscopy. Combination of these techniques provides a comprehensive understanding of the composition of the materials at both aspects of the bulk and molecule scale.

3.1 Thermogravimetric Analysis

Thermogravimetric analysis (TGA) was used to understand the basic composition of the lignin CELF residues compared to their biomass feedstocks. Figure 1 provides TGA and DTG data for maple wood, bagasse, poplar wood and their treated residues (all CELF lignins plus poplar wood also treated by enzyme). According to TGA curves, all samples are relatively stable before 215 °C, but a quick weight loss between 215 and 365 °C, and then become much slower above 365 °C. The reducing amount of biomass weight above 600 °C decreases after CELF treatment indicating removal of carbohydrates and formation of biochar and ash.[24] Enzyme may degrade some thermally stable cellulose, hemicellulose or lignin which leads to the CELF lignin of poplar wood losing more weight with enzyme treatment than without it. From DTG curves, samples show peaks below 100 °C indicate presence of moisture loss.[25] Major feature is the peak at ~340°C due to cellulose decomposition. [24] This cellulose peak greatly reduced with CELF treatment, but still present indicating some cellulose remains bound with the lignin. The shoulder of the cellulose peak is assigned to hemicellulose.[26] Interestingly, a broad feature centered at approximately 240-260 °C appears after CELF treatment likely attributable to hemicellulose or amorphous cellulose – or something else such as partly hydrolyzed cellulose. This low temperature feature is especially apparent in poplar wood (even more obvious after treated by enzyme) and bagasse; less so in maple wood. The peak is significant in the enzyme treated poplar wood, indicating significant hemicelluloses remain in the solid residue. The other major feature occurs at approximately 450 °C, which can be attributed to lignin, percentage of which increases after treatment in all cases due to flushing out of carbohydrates.[27] For poplar wood, the peaks of cellulose and lignin decrease after enzyme treatment which confirms the enzyme degrades cellulose and lignin. Compare all the feed materials from DTG data, poplar wood has higher percentage of cellulose which is also lost more than other materials. Maplewood leaves the highest percentage of cellulose. In summary, the TGA data seems to indicate that cellulose and hemicellulose are greatly reduced during treatment, but not completely removed from the feed biomass.

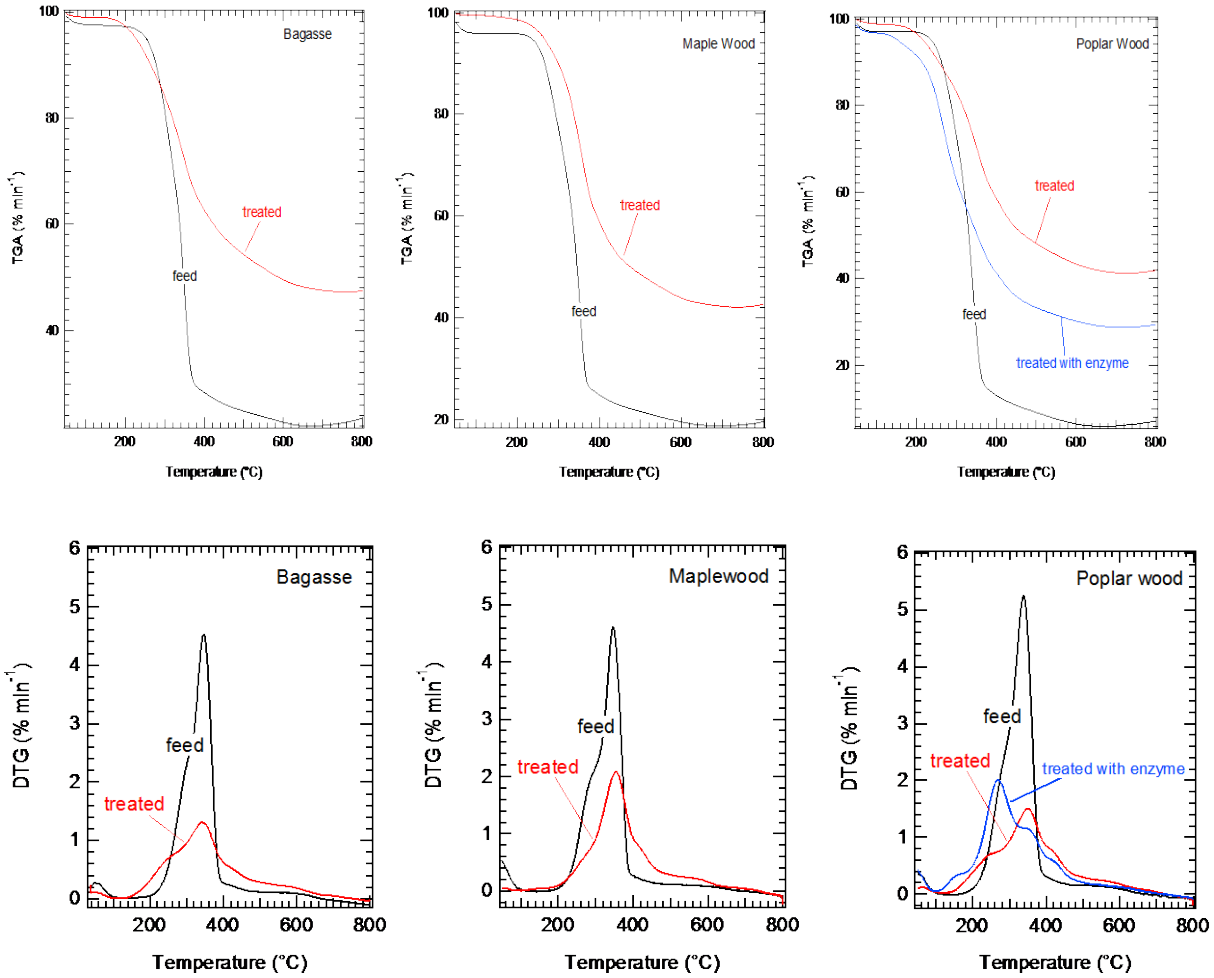

Figure 1. TGA and DTG of maplewood, bagasse, poplar wood and their treated residues.

3.2 X-ray diffraction

After studying the composition of the lignins and biomass materials with TGA, we determined the cellulose crystallinity using X-ray diffraction. Crystallinity of cellulose is one of the key factors which affect the rates of biodegradation of lignocellulosic biomass.[28, 29] Figure 2 shows XRD spectra of lignins and their treated materials. For all the raw materials, the spectra present two identical peaks ($2\theta = 16°$ and 23°) due to the crystal structure of cellulose. He J et al. separated four crystalline peaks (101, 10-1, 002 and 040) for the diffractogram of cellulose to measure its crystallinity index (CI). [30] CI is calculated as integrated area of all crystalline peaks by the total integrated area. The peak fitting of bagasse is shown as an example of the positions of the

individual peaks in Figure 3. The area and CI are listed in Table 1 showing CI of maple wood is the largest which indicates it has less accessible amorphous portion. Based on Kumar and Wyman's study, maple wood is harder to be hydrolyzed cellulosic substrates from the aspect of cellulose crystallinity. [28, 29] The two distinct peaks turn to one broad peak indicating decrease in the crystallinity of cellulose and formation of amorphous cellulose. The XRD analysis is consistent with TGA on the decrease of cellulose.

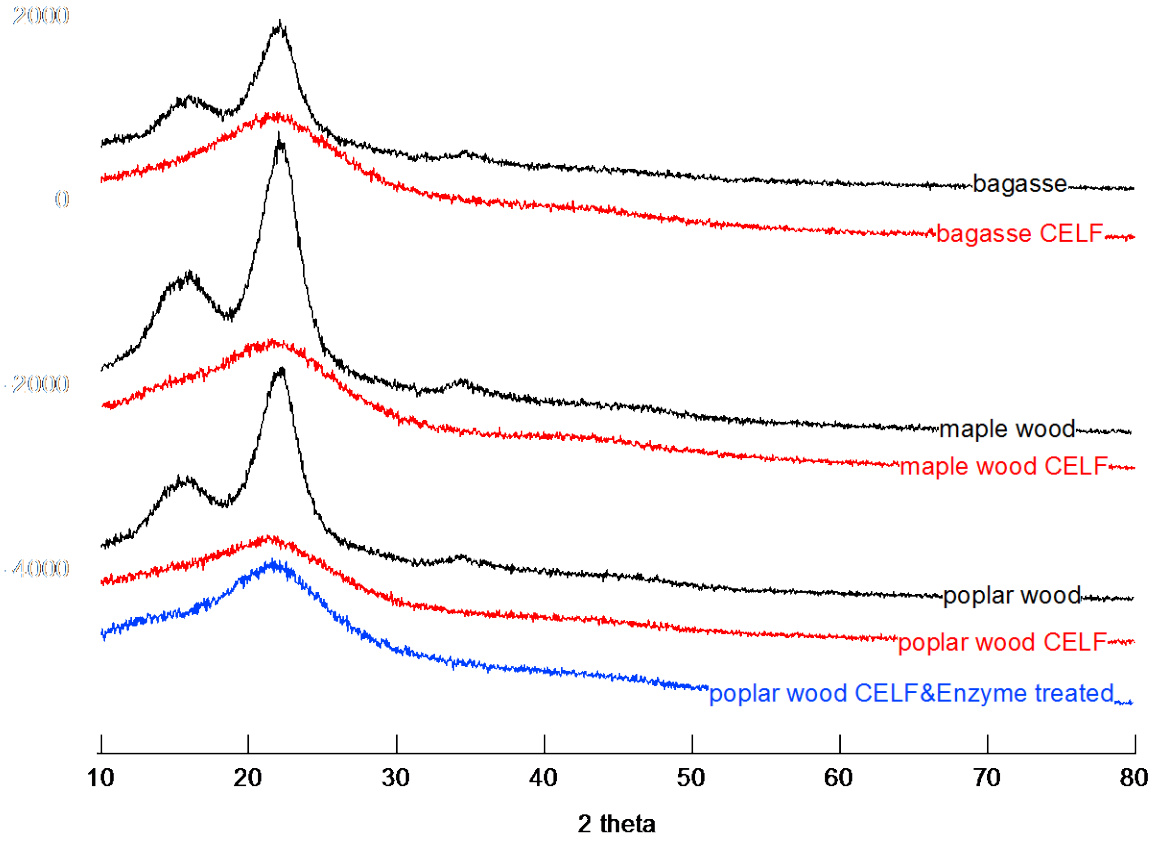

Figure 2. XRD spectra of lignins and their treated materials.

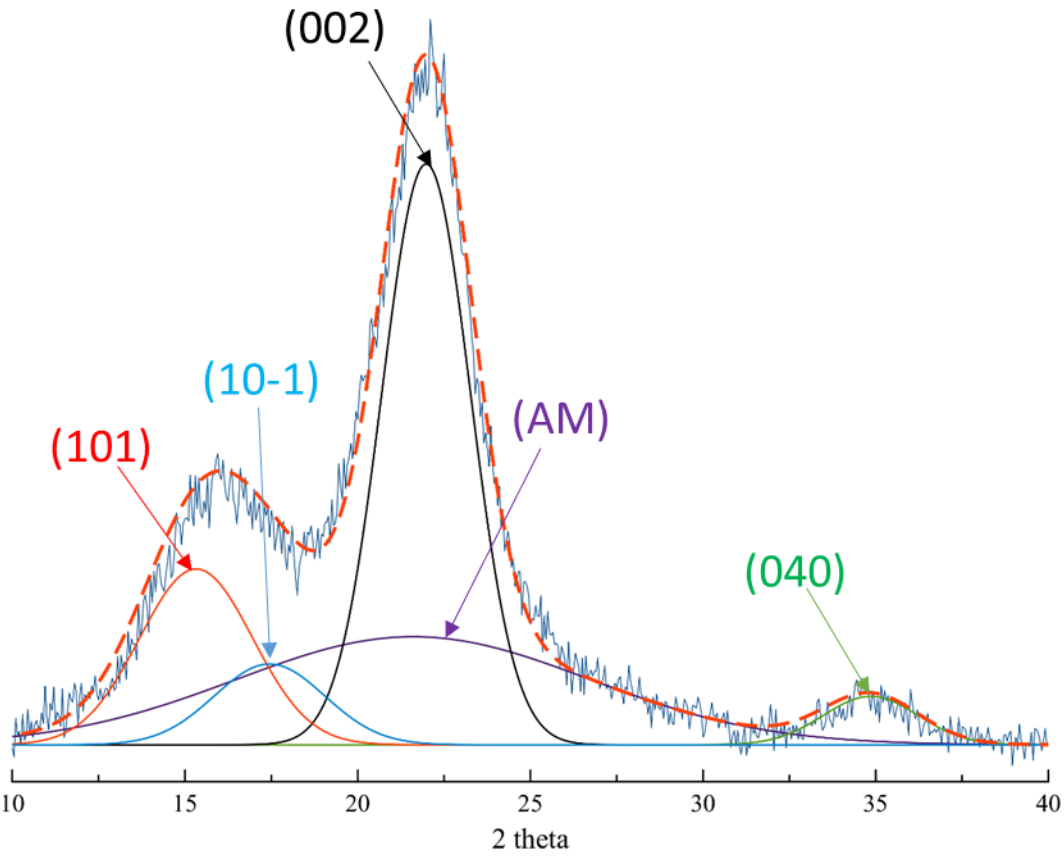

Figure 3. Peak fitting of XRD spectrum of bagasse and its assignment.

Table 1. Integrated areas of crystalline and amorphous peaks and evaluated CI

	101	10-1	002	040	Amorphous	CI
Bagasse	1426	638.189	3689	329	2734	0.69
Poplar wood	2271	1381.15	5563	329	2933	0.765
Maple wood	3721	2839.01	7266	270.2	2560	0.846

3.3 Infrared Spectroscopy

TGA and XRD analysis together indicate the decrease in the cellulose content and transformation to amorphous cellulose and lignin in all biomass lignin residue materials. Then we investigated the chemical molecular composition of the residues compared to the biomass feed stocks using

FTIR spectroscopy. Figure 3 shows the infrared spectra of bagasse, maple wood, poplar wood, their CELF treated residues and poplar wood after enzyme treatment. Table 1 lists infrared band positions and assignments from literatures. The spectra of the feed stocks basically possess similar features as regular wood materials, [31, 32, 33] small peaks around 900 cm^{-1} assigned to lignin and carbohydrates, prominent peaks centered at 1030 cm^{-1} attributed to cellulose or hemicellulose with shoulders at 990 cm^{-1} attributed to lignin, a broad superposition with discrete absorptions between 1111 and 1788 cm^{-1}, C–H stretch in methyl and methylene groups from 2800 to 3000 cm^{-1} and broad OH region (3000-3600 cm^{-1}). The intensity and area of the carbohydrates peaks at 1030 cm^{-1} are largest which indicates cellulose and hemicellulose composite most of the biomass, it's consistent with Cai et al 's report that xylan and glucan make up of 55% raw maple wood, while lignin only has 25% in it.[20]

The intensity of peaks are compared to determine the chemical change after CELF or enzyme treatment. A bunch of peaks increasing intensity are observed in the spectra of treated materials. Bands at around 855 cm^{-1} and 1161 – 1720 cm^{-1} assigned to lignin increase in intensity indicating the transfer of domination of cellulose to lignin consistent with the TGA analysis. Other evidence includes the broad carbohydrate band at 1034 cm^{-1} becomes two separate distinct bands and the O-H band gets broader due to the main content of lignin. [34] The band at 1728 cm^{-1} attributed to hemicellulose in the spectra of feed stocks decreases in intensity indicative of removal of hemicellulose. However, the C-H broad band at 2895 cm^{-1} turns to two sharp peaks of hemicellulose probably because of degradation of cellulose to hemicellulose. [34] For CELF treated maple wood, the band present at 1161 cm^{-1} attributed to lignin and cellulose increases more than other treated materials consistent with the TGA analysis that maple wood leaves higher percentage of cellulose. It testifies that maple wood is the hardest to be hydrolyzed among the three woods in agreement with XRD study. Peaks associated with amorphous cellulose (at around 1216 cm^{-1}) decrease more for maple wood CELF lignin and poplar wood enzyme lignin than other treated materials, which indicates amorphous cellulose in maple wood is easier to hydrolyze with CELF as well as poplar wood to enzyme & CELF. In general, poplar wood is more resistant to CELF and enzyme than others to extract lignin from the intensity decrease at 1240 – 1599 cm^{-1} region.

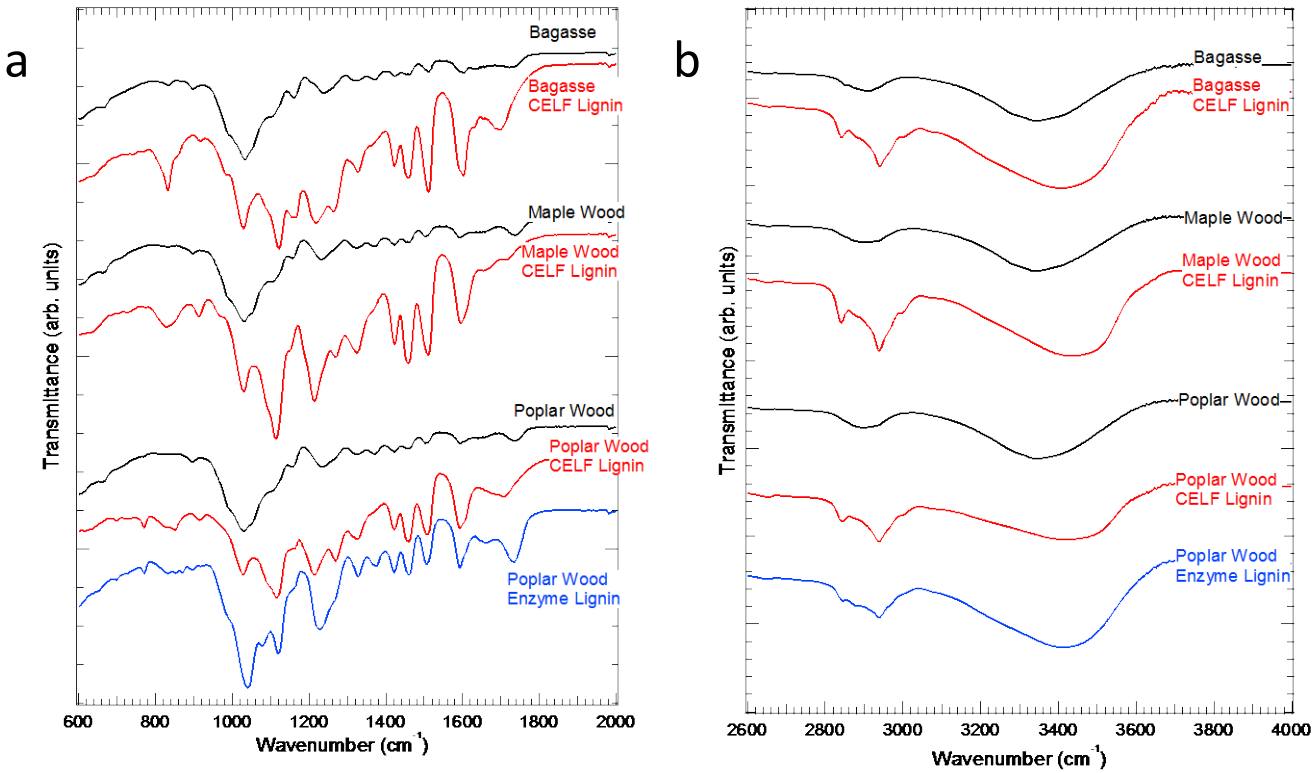

Figure 3. Infrared spectra of biomass and their treated left lignins in (a) fingerprint region (600-2000 cm^{-1}) and (b) OH region (2600-4000 cm^{-1}).

Table 1. Infrared band positions and assignment for bagasse, maple wood, poplar wood, their CELF lignin and CELF & enzyme lignin of poplar wood

Bagasse (cm^{-1})	Bagasse CELF Lignin (cm^{-1})	Maple wood (cm^{-1})	Maple wood CELF lignin (cm^{-1})	Poplar wood (cm^{-1})	Poplar wood CELF lignin (cm^{-1})	Poplar wood enzyme lignin (cm^{-1})	Assignment	Reference
667		664		669	700	700	unknown	
					768	770		
835	834		827		824	824	C-H deformation out of plane, aromatic ring	2
	863sh		856sh		851sh	851sh	C-H deformation out of plane, aromatic ring	2

Table 1. (Continued)

899	915	895	911	897	918	893	C-H deformation out of plane, aromatic ring, lignin, anomeric C-groups, C1-H deformation, of Cellulose, hemicellulose	2, 3, 32
993sh	976	991sh	970sh		988sh	991sh	aromatic CH in plane deformation	32
1034		1030		1030			Cellulose/hemicellulose C-O	3
	1022		1028		1026	1038	Aromatic C-H in plane deformation	2
	1086sh		1086sh		1090sh	1080sh	C-O deformation, secondary alcohol and aliphatic ether, lignin and carbohydrate	2
1109		1103		1101			Cellulose/hemicellulose C-O	1
	1119		1119		1119	1117	Aromatic C-H in plane deformation	2
1161	1161	1155	1151sh	1159	1161sh	1159sh	Aromatic C-H in plane deformation, cellulose C-O	2
1240	1219	1227	1216	1229	1209	1227	Aryl ring breathing with C=O stretch	2
	1268		1268		1265	1269sh	Aryl ring breathing with C-O stretch	2
1323	1332	1326	1323	1330	1327	1327	Aryl ring breathing with C-O stretch	2
1369	1365	1371	1358	1371	1373sh	1369	O-CH3 C-H deformation symmetric	2
1422	1426	1421	1420	1421	1422	1421	O-CH3 C-H deformation, asymmetric	2

Table 1. (Continued)

1458	1455	1462	1459	1460	1456	1458	C-H deformation, asymmetric	2
1512	1511	1503	1511	1501	1506	1505	aryl ring stretching, asymmetric	2
1599	1601	1593	1598	1591	1591	1593	aryl ring stretching, symmetric	2
	1637		1653			1657	ring conjugated C=C stretch of coniferyl/sinapyl alcohol	2
	1695		1718		1709	1736	C=O stretch, unconjugated ketone, carboxyl, and ester groups	2
1728		1737		1734			hemicellulose	32
	2840		2837		2841	2843	C-H stretch O-CH3 group	2
2897	2876	2902	2882	2897	2886	2878	C-H stretch in methyl and methylene groups	2
	2937		2937		2934	2934	C-H stretch methyl and methylene groups	2
	2999		2999		2997			
3341	3413	3352	3430	3333	3449	3406	O-H stretch	2

3.4 Raman Spectroscopy

Raman spectroscopy is used as a complementary technology after infrared spectroscopy provides information about chemical groups. Figure 4 provides Raman spectra of biomass and the lignin residues after CELF treatment. Table 2 lists Raman band positions along with literature-based assignments. For the raw materials, the bands at the region 374-574 cm^{-1} are due to vibrations from

carbohydrates and lignins. Karla et al assigned bands around 350 cm^{-1} to τ (CCO), 377 and 410 cm^{-1} to δ (CCC),δ (CO), δ (CCO), ring deformation, 433 and 456 cm^{-1} to δ (CCC), δ (CCO), ring deformation, 492 and 517 cm^{-1} to δ (COC) glycosidic bond and 574 cm^{-1} to δ (COC) ring mode of carbohydrates. [35] Bands below 900 cm^{-1} are attributed to skeletal deformation of aromatic rings, substituent groups and side chains from lignins. Bands at around 980 cm^{-1} for bagasse and poplar wood correspond to CCH and -HC=CH- deformation of lignins.[31] Cael et al assigned several bands at the range 1034 – 1159 cm^{-1} to carbohydrates indicated by CO, CC, CCO and etc. bands.[36] Bands between 1266 and 1447 cm^{-1} are due to presence of lignins and carbohydrates.[31] The intensity of the spectra gets weaker after treatment, presumably because the CELF treated lignins absorb more laser and inhibit scattering of it. In comparison with infrared spectra, Raman spectra have fewer featured peaks especially for the lignins after treatment. For bagasse, most bands are gone except for a small band at 576 cm^{-1} indicating left of carbohydrates, and two small lignin bands at 1602 and 1634 cm^{-1}. A broad band forms centered at 1232 cm^{-1} probably due to the overlap of left over carbohydrates and lignin bands. The spectrum of treated maple wood is almost flat other than a small lignin band, which isn't reasonable from the TGA and Infrared study. Maybe because Raman spectroscopy isn't sensitive to maple wood material. Spectra of poplar wood are better resolved than other materials. The bands below 1200 cm^{-1} decrease substantially after CELF treatment and continue to decrease when treated by carbohydrate enzyme, indicating certain amount of carbohydrates remain when treated by CELF. The spectrum of CELF treated poplar wood present a similar broad band centered at 1272 cm^{-1} to that of CELF treated bagasse. After enzyme treatment, it mainly leaves lignin bands conforming the hypothesis of the broad band in the spectrum of CELF treated bagasse.

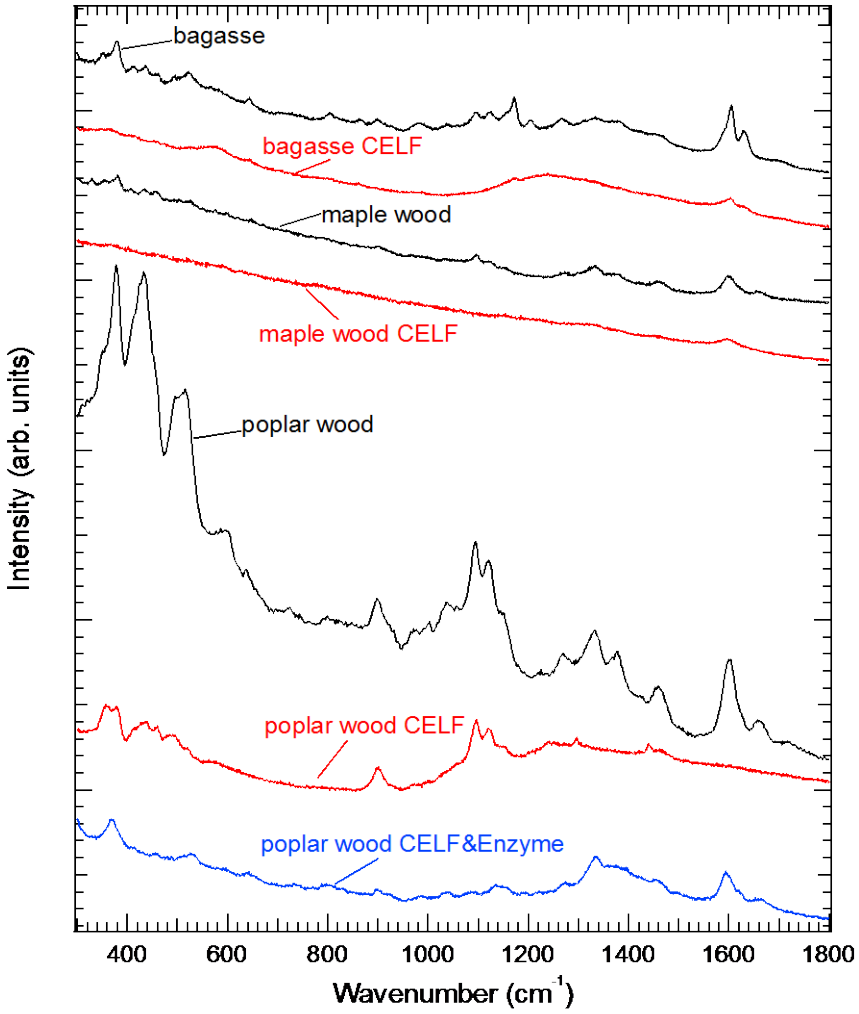

Figure 4. Raman spectra of biomass and CELF or CELF & enzyme lignin.

Table 2. Raman band positions and assignments for biomass and their treated left lignin samples

Bagasse (cm^{-1})	Bagasse CELF Lignin (cm^{-1})	Maple wood (cm^{-1})	Maple wood CELF lignin (cm^{-1})	Poplar wood (cm^{-1})	Poplar wood CELF lignin (cm^{-1})	Poplar wood enzyme lignin (cm^{-1})	Assignment	Reference
347sh		354		348	354	368	skeletal deformation of aromatic rings, substituent groups, and side chains; τ (CCO)	31, 35

Table 2 (continued)

377		380		378	378		skeletal deformation of aromatic rings, substituent groups, and side chains; δ (CCC),δ (CO), δ (CCO), ring deformation	31, 35
410		411					skeletal deformation of aromatic rings, substituent groups, and side chains; δ (CCC), δ (CO), δ (CCO), ring deformation	31, 35
433		431					skeletal deformation of aromatic rings, substituent groups, and side chains; δ (CCC), δ (CCO), ring deformation	31, 35
456		457	432		438		skeletal deformation of aromatic rings, substituent groups, and side chains; δ (CCC), δ (CCO), ring deformation	31, 35
					457		skeletal deformation of aromatic rings, substituent groups, and side chains	31, 35
492sh				496	496		skeletal deformation of aromatic rings, substituent groups, and side chains; δ (COC) glycosidic	31, 35
517		523		516	520	528	skeletal deformation of aromatic rings, substituent groups, and side chains; δ (COC) glycosidic	31, 35
574	576	543		597	578		skeletal deformation of aromatic rings, substituent groups, and side chains; δ (COC) ring	31, 35
636				636		639	skeletal deformation of aromatic rings, substituent groups, and side chains	31, 35

Table 2 (continued)

			725			CCO, COC, OCO, HCC Cellulose	36
			744		738		
796			796		797	skeletal deformation of aromatic rings, substituent groups, and side chains	31, 35
866							
897		903	900	900	898	skeletal deformation of aromatic rings, substituent groups, and side chains; δ (C(1) H(β))	31, 35
982			971		982	CCH and -HC=CH- deformation	31, 35
			1003			CO, CC, CCO Cellulose	36
1034			1037		1037	CO, CC, CCO, HCO, HCC, cellulose	36
1092		1096	1093	1095	1085	CO, CC, COH -cellulose	36
1123		1123	1119	1120	1137	C-O of aryl-O-CH3 and aryl-OH or/and	31, 35
						CO, CC, CCO, COH Cellulose	36
1159			1152	1151		out of phase C-C-O stretch of phenol or/and	31, 35
						CO, CC, CCC, CCO, COH Cellulose	36
1170	1176					a mode of coniferaldehyde/sinapaldehyde	31, 35
1206	1232		1225	1241		Unassigned/ a phenol mode	
1266		1273	1268	1295	1272	aryl-O of aryl-OH and aryl-O-CH3; guaiacyl/syringyl ring (with C=O group) mode or/and HCC and HCO bending	31, 35, 37

Table 2 (continued)

1331		1332		1332		1332	aliphatic O-H bend or/and HCC and HCO bending	31, 35, 37
1379		1376		1378		1398	C-H bend in R3C-H or/and HCC, HCO, and HOC bending	31, 35, 37
1447		1459		1460	1439	1459	O-CH3 deformation; CH2 scissoring; guaiacyl/syringyl ring vibration or/and HCH and HOC bending	31, 35, 37
					1464sh		?	
1603	1602	1598	1603	1600		1594	aryl ring stretching, symmetric	31, 35, 37
1632sh	1634	1653		1662		1664	ring conjugated C=C stretch of coniferaldehyde/ sinapaldehyde	31, 35, 37

4. Conclusions

Bagasse, maple wood and poplar wood were obtained and analyzed together with their residues treated by CELF method. TGA showed removal of carbohydrates and formation of char and ash after CELF treatment. DTG reveals presence of cellulose, hemicellulose, lignin in the feedstock and small amount of carbohydrates retain after CELF treatment. XRD confirms cellulose decrease and indicates maple wood the hardest to be hydrolyzed among the three woods. Infrared spectroscopy is consistent with TGA analysis and present poplar wood decomposes less than other woods. Raman spectroscopy confirms remain of carbohydrates after CELF treatment in poplar wood due to the intensity of carbohydrate bond decrease after a further enzymatic treatment. The combination of the characterization techniques provides a powerful tool to understand the CELF processing by studying the solid materials and gives insight on the best candidate for CELF treatment.

5. Acknowledgements

NSF (award # ECE-1342320) provided partial support for the WPI component of this work. NREL donated air-dried woods materials.

6. References

(1) Smith, M. D.; Cheng, X.; Petridis, L.; Cai, C. M.; Wyman, C. E.; Smith, J. C. **2016**, 1268–1277.

(2) Charles E. Wyman; George Huber. **2009**, 105–107.

(3) Cai, C. M.; Nagane, N.; Kumar, R.; Wyman, C. E. *Green Chem.* **2014**, *16*, 3819–3829.

(4) Long, J.; Zhang, Q.; Wang, T.; Zhang, X.; Xu, Y.; Ma, L. *Bioresour. Technol.* **2014**, *154*, 10–17.

(5) Singh, R.; Shukla, A.; Tiwari, S.; Srivastava, M. *Renew. Sustain. Energy Rev.* **2014**, *32*, 713–728.

(6) Nguyen, T. Y.; Cai, C. M.; Kumar, R.; Wyman, C. E. **2015**, 1716–1725.

(7) Lynd, L. R.; Wyman, C. E.; Gerngross, T. U. **1999**.

(8) Nguyen, T. Y.; Cai, C. M.; Osman, O.; Kumar, R.; Wyman, C. E. *Green Chem.* **2016**, 1581–1589.

(9) Rubin, E. M.; Himmel, M. E.; Ding, S.; Johnson, D. K.; Adney, W. S. *Nature* **2007**, *454* (February), 804–807.

(10) Agbor, V. B.; Cicek, N.; Sparling, R.; Berlin, A.; Levin, D. B. *Biotechnol. Adv.* **2011**, *29* (6), 675–685.

(11) Watkins, D.; Hosur, M.; Tcherbi-narteh, A.; Jeelani, S. *Integr. Med. Res.* **2014**, *4* (1), 26–32.

(12) Yuan, T.; Sun, R. *Chem Technol Biotechnol* **2012**, No. October.

(13) Ragauskas, A. J.; Beckham, G. T.; Biddy, M. J.; Chandra, R.; Chen, F.; Davis, M. F.; Davison, B. H.; Dixon, R. A.; Gilna, P.; Keller, M.; Langan, P.; Naskar, A. K.; Saddler, J. N.; Tschaplinski, T. J.; Tuskan, G. A.; Wyman, C. E.; Ragauskas, A. J.; Beckham, G. T.; Biddy, M. J.; Chandra, R.; Chen, F.; Davis, M. F.; Davison, B. H.; Dixon, R. A.; Gilna, P.; Keller, M.; Langan, P.; Naskar, A. K.; Saddler, J. N.; Tschaplinski, T. J.; Tuskan, G. A.; Wyman, C. E. *Science (80-.).* **2014**, *344* (May).

(14) Chapple, C.; Ladisch, M.; Meilan, R. *Nat. Biotechnol.* **2007**, *25* (7), 746–748.

(15) Graham, J. E.; Clark, M. E.; Nadler, D. C.; Huffer, S.; Chokhawala, H. a; Rowland, S. E.; Blanch, H. W.; Clark, D. S.; Robb, F. T. *Nat. Commun.* **2011**, *2*, 375.

(16) Yang, B.; Wyman, C. E. **2008**, 26–40.

(17) Fan, L. T. .

(18) Sousa, C.; Chundawat, S. P. S.; Balan, V.; Dale, B. E. **2009**.

(19) Liu, C.; Wyman, C. E. **2003**, 5409–5416.

(20) Cai, C. M.; Zhang, T.; Kumar, R.; Wyman, C. E. *Green Chem.* **2013**, 3140–3145.

(21) Hult, E.; Iversen, T.; Sugiyama, J. **2003**, 103–110.

(22) Smith, M. D.; Petridis, L.; Cheng, X.; Smith, J. C. *Phys. Chem. Chem. Phys.* **2016**, *18*, 6394–6398.

(23) Park, S.; Baker, J. O.; Himmel, M. E.; Parilla, P. a; Johnson, D. K. *Biotechnol. Biofuels* **2010**, *3* (1), 10.

(24) Zhou, H.; Long, Y.; Meng, A.; Chen, S.; Li, Q.; Zhang, Y. *RSC Adv.* **2015**, *5*, 26509–26516.

(25) Zhang, M.; Resende, F. L. P.; Moutsoglou, A.; Raynie, D. E. *J. Anal. Appl. Pyrolysis* **2012**, *98*, 65–71.

(26) Yang, H. **2007**, *86*, 1781–1788.

(27) Cai, J.; Wu, W.; Liu, R. *Green Chem.* **2013**, 1331–1340.

(28) Kumar, R.; Wyman, C. E. *Bioresour. Technol.* **2009**, *100* (18), 4193–4202.

(29) Prasad, D.; Ankit, M. *3 Biotech* **2015**, 597–609.

(30) He, J.; Cui, S.; Wang, S. **2007**.

(31) Cyril Heitner, Don Dimmel, J. S. *CRC Press* **2010**, 103–136.

(32) Kobayashi, N.; Okada, N.; Hirakawa, A.; Sato, T.; Kobayashi, J.; Hatano, S.; Itaya, Y.; Mori, S. **2009**, 373–379.

(33) R. BODÎRLĂU, C. A. T. *Rom. J. Phys.* **2009**, *54* (July 2007), 93–104.

(34) Fan, M.; Dai, D.; Huang, B. **2012**, No. InTech.

(35) Schenzel, K.; Fischer, S. *Cellulose* **2001**, 49–57.

(36) John J. Cael, Jack L. Koenig, and J. B. Carbohydrate Research 1973.

(37) Agarwal, U. P.; Ralph, S. A. **1997**, *51* (11), 1648–1655.